Nano Research

ISSN 1998-0124 CN 11-5974/O4
https://doi.org/10.26599/NR.2026.94908732

Research Article

Decoupling local renin-angiotensin system inhibition from systemic effects: A neutrophil-mimetic, ROS-responsive nanocarrier for precision therapy of myocardial ischemia/reperfusion injury

Wusiman Yakufu[1,2,§], Yuekai Shi[3,§], Jinfeng Gao[3,§], Ayitongguli Aimaiti[1,2], Nueraili Kadi[1,2], Qiyu Li[3], Miribanguli Alifu[1,2], Aikebaier Yasen[5], Muhetaer Wubuli[1,2], Yang Pang[1,3], Su Li[3], Zhenzhen Huang[1,2], Rongrong Lu[1,2], Maimaitiaili Tuerxun[1,2], Reyimai Mutailipu[1,2], Abulimiti Jamali[1,2], Wumaierjiang Kelimu[1,2], Xianglin Tang[3], Qibing Wang[3], Yuqiong Chen[4](✉), Abudureheman Mijiti[1,2](✉), Zheyong Huang[3](✉), Junbo Ge[3]

[1] Kashi Prefecture Second People's Hospital, Kashi 844000, China

[2] The First Affiliated Hospital of Kashi University, Kashi 844000, China

[3] Department of Cardiology, Zhongshan Hospital, Shanghai Institute of Cardiovascular Diseases, Fudan University, Shanghai 200032, China

[4] The Affiliated Suzhou Hospital of Nanjing Medical University, Suzhou 215000, China

[5] Kashi University School of Medicine, Kashi 844000, China

[§] Wusiman Yakufu, Yuekai Shi, and Jinfeng Gao contributed equally to this work.

Nano Res., **Just Accepted Manuscript** • https://doi.org/10.26599/NR.2026.94908732

https://www.sciopen.com/journal/1998-0124 on Apr. 10, 2026

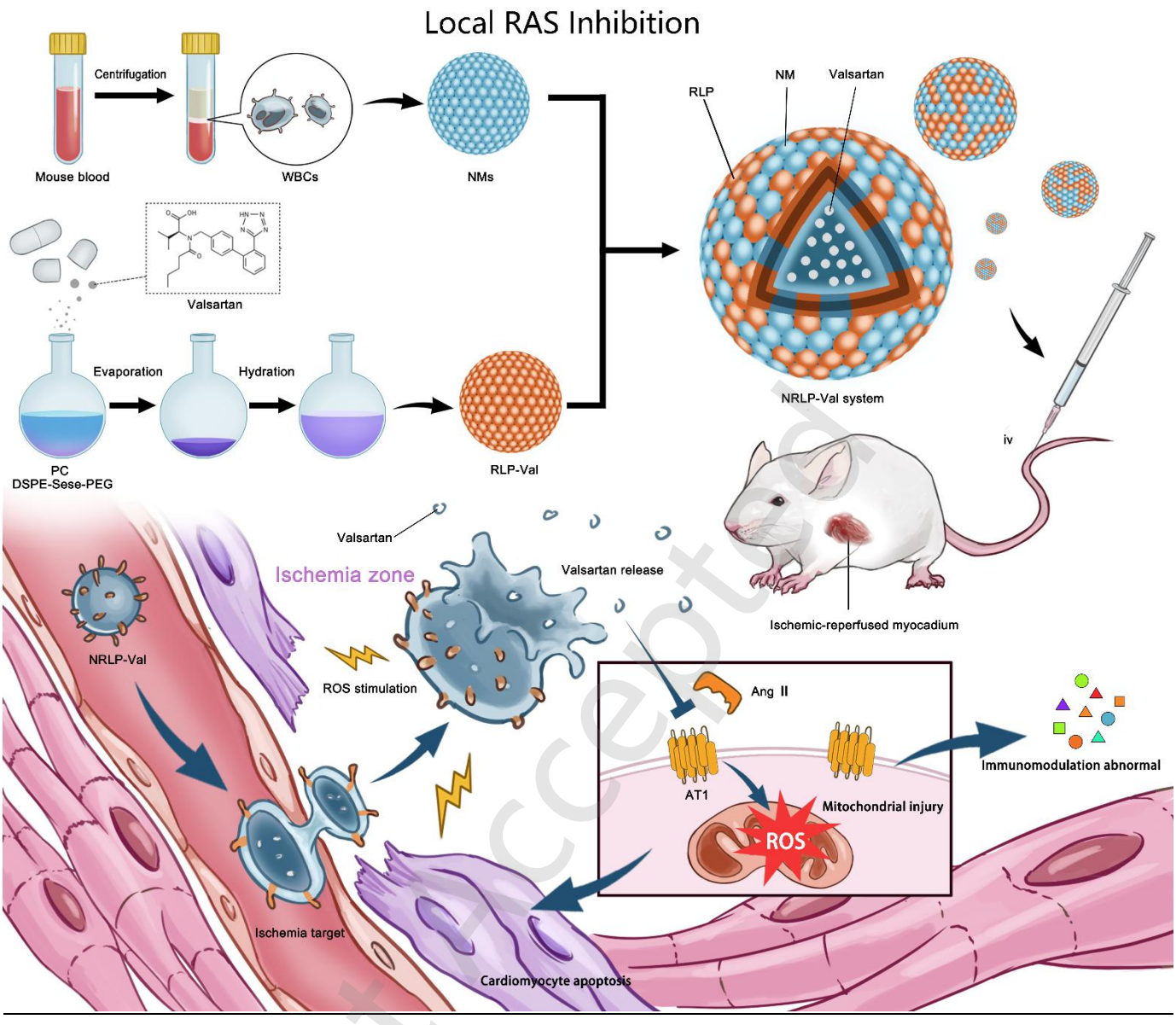

Schematic illustration of the fabrication of NRLP-Val and its mechanism for targeted therapy of myocardial ischaemia/reperfusion injury. Neutrophil membrane vesicles were fused with a reactive oxygen species (ROS)-responsive lipid nanoparticle core loaded with valsartan (NRLP-Val). This biomimetic nanocarrier preferentially accumulated in the ischaemic myocardium and released valsartan in response to an elevated ROS microenvironment, thereby selectively inhibiting the local renin-angiotensin system to ameliorate myocardial ischaemia/reperfusion injury.

Nano Research

Open Access

Review Article/Research Article Please choose on

Decoupling local renin-angiotensin system inhibition from systemic effects: A neutrophil-mimetic, ROS-responsive nanocarrier for precision therapy of myocardial ischemia/reperfusion injury

Wusiman Yakufu[1,2,§], Yuekai Shi[3,§], Jinfeng Gao[3,§], Ayitongguli Aimaiti[1,2], Nueraili Kadi[1,2], Qiyu Li[3], Miribanguli Alifu[1,2], Aikebaier Yasen[5], Muhetaer Wubuli[1,2], Yang Pang[1,3], Su Li[3], Zhenzhen Huang[1,2], Rongrong Lu[1,2], Maimaitiaili Tuerxun[1,2], Reyimai Mutailipu[1,2], Abulimiti Jamali[1,2], Wumaierjiang Kelimu[1,2], Xianglin Tang[3], Qibing Wang[3], Yuqiong Chen[4]✉, Abudureheman Mijiti[1,2]✉, Zheyong Huang[3]✉, and Junbo Ge[3]

1 Kashi Prefecture Second People's Hospital, Kashi 844000, China

2 The First Affiliated Hospital of Kashi University, Kashi 844000, China

3 Department of Cardiology, Zhongshan Hospital, Shanghai Institute of Cardiovascular Diseases, Fudan University, Shanghai 200032, China

4 The Affiliated Suzhou Hospital of Nanjing Medical University, Suzhou 215000, China;

5 Kashi University School of Medicine, Kashi 844000, China

§Wusiman Yakufu, Yuekai Shi, and Jinfeng Gao contributed equally to this work.

Received: 17 January 2026; **Revised:** 9 April 2026; **Accepted:** 10 April 2026

✉Address correspondence to Abudureheman Mijiti, 18999199903@163.com; Zheyong Huang. zheyonghuang@126.com; Yuqiong Chen, cosmoscyq@163.com

Cite this article: *Nano Research*, 2026, 19, 94908732 https://doi.org/10.26599/NR.2026.94908732

ABSTRACT: Myocardial ischaemia/reperfusion (MI/R) injury causes adverse cardiac remodelling by activating the local renin-angiotensin system (RAS). In this study, we engineered a neutrophil membrane-biomimetic nanocarrier that facilitates the reactive oxygen species (ROS)-responsive release of valsartan (NRLP-Val) to precisely target MI/R injury. This design leverages neutrophil-derived adhesion molecules for targeted delivery to the inflamed myocardium and promotes ROS-triggered drug release at the infarct site. NRLP-Val effectively traversed activated endothelium and protected cardiomyocytes from angiotensin II-induced mitochondrial dysfunction and apoptosis in vitro. In vivo, NRLP-Val demonstrated superior cardiac accumulation and a dose-dependent therapeutic profile in a murine MI/R model. Notably, the 8 mg/kg dose achieved maximal efficacy, which was statistically equivalent to that of the 12 mg/kg dose, in acutely reducing the infarct size, oxidative stress, apoptosis, and inflammation. Long-term treatment with 8 mg/kg NRLP-Val significantly inhibited fibrosis, improved ventricular remodelling, and restored cardiac function at 28 days, outperforming the non-targeted controls and free valsartan. The platform exhibited an excellent safety profile. Therefore, 8 mg/kg NRLP-Val is a promising and clinically translatable strategy for achieving potent local RAS inhibition without systemic compromise, offering a novel targeted therapeutic approach for ischaemic heart disease.

KEYWORDS: myocardial ischaemia/reperfusion injury, targeted drug delivery, neutrophil-mimetic nanocarrier, ROS-responsive, local renin-angiotensin system inhibition

1 Introduction

Although the mortality rate of acute myocardial infarction (AMI) has declined over the past two decades, it remains a leading cause of death worldwide[1]. Reperfusion therapy effectively salvages ischaemic myocardia and reduces mortality; however, the subsequent reperfusion injury can trigger ventricular remodelling, potentially leading to heart failure[2, 3]. This significantly affects the patients' long-term quality of life and prognosis[4]. Among the pathogenic factors, activation of the renin-angiotensin system (RAS), particularly excessive

activation within the myocardium, is a key mechanism underlying post-reperfusion ventricular remodelling [5].

The significant activation of the local cardiac RAS following acute myocardial infarction was confirmed by elevated levels of angiotensin II (Ang II)[6-10]. An increase in Ang II can induce mitochondrial dysfunction, cardiomyocyte apoptosis, and inflammatory cytokine infiltration, collectively accelerating ventricular remodelling[11-14]. Therefore, the targeted inhibition of cardiac RAS activity is a pivotal therapeutic strategy for mitigating ventricular remodelling, alleviating reperfusion injury, and reducing the incidence of heart failure[15, 16]. However, the current mainstream RAS inhibitors, including angiotensin-converting enzyme inhibitors, angiotensin receptor blockers, and angiotensin receptor-neprilysin inhibitors, face clinical challenges in achieving efficient and sufficient suppression of cardiac RAS activity. These challenges occur due to dosage limitations after reperfusion, potential risks to haemodynamic stability, and a lack of tissue specificity[17, 18]. Consequently, there is an urgent need to develop novel drug delivery systems capable of actively targeting the heart. These systems will deliver adequate doses of drugs precisely to the ischaemic area and maintain haemodynamic stability, thereby achieving effective local RAS inhibition.

Recent advancements in cell membrane biomimetic modification technology and microenvironment-responsive delivery systems provide new avenues for efficient and precise drug targeting[19-22]. We previously successfully constructed biomimetic liposomes derived from platelet, erythrocyte, and macrophage membranes, and developed drug carrier systems characterised by pH-responsive release[9, 23-26]. These biomimetic liposomes inherit the chemotactic and adhesive properties of their source cells, demonstrating excellent targeting capabilities, prolonged circulation, and immune evasion. Additionally, the microenvironment-responsive systems facilitate controlled drug release at lesion sites, effectively enhancing local drug concentration[27-29].

In the present study, we developed a novel targeted delivery platform using reactive oxygen species (ROS)-responsive liposomes (RLPs) modified with neutrophil membranes and loaded with valsartan (NRLP-Val; Figure 1). This system leverages the innate directional chemotaxis and adhesive properties of neutrophils towards inflammatory sites, combined with an intelligent drug-release mechanism triggered by a high-ROS microenvironment. Following AMI, the heart exhibits a pronounced local inflammatory response, exacerbated by a reperfusion-induced ROS burst[30-32]. Using this pathophysiology, NRLP-Val actively targets the infarcted myocardium in a mouse model of ischaemia-reperfusion injury without compromising systemic haemodynamics. Upon arrival, releases a high local dose of valsartan to mitigate mitochondrial damage, suppress cardiomyocyte apoptosis, and modulate immune responses, ultimately improving ventricular remodelling and restoring cardiac function.

2 Experimental

2.1 Neutrophil membrane isolation

Neutrophils were isolated from the blood of lipopolysaccharide (LPS)-treated mice (1.5 mg/kg, 6 h after injection) using Percoll gradient centrifugation[33]. Cells were lysed using a Dounce homogeniser with 20 strokes. The lysate was subsequently clarified through differential centrifugation, initially at 20,000 × g for 25 **min,** followed by ultracentrifugation of the supernatant at 100,000 × g for 35 **min**, with both steps conducted at 4 °C. The resulting crude membrane pellet was collected and washed twice with a 0.2 mM EDTA.

2.2 NRLP-Val synthesis

RLPs were prepared using the lipid film rehydration method[34]. Specifically, the lipid components, SPC (9 mg), DSPE-SeSe-PEG2000 (1.5 mg), and cholesterol (1.5 mg), were dissolved in 12 mL of chloroform and dried under reduced pressure to form a thin film. The film was then hydrated with 12 mL of distilled water at 37 **°C** for 15 min, followed by sonication at 52 kHz and 100 W for 15 min. The resulting suspension was homogenised through sequential extrusion (20 times each) using 1.0, 0.4, and 0.2 **μm** polycarbonate membranes with a LiposoFast apparatus, yielding a clear liposomal solution. NRLP-Val was prepared by fusing neutrophil membrane vesicles (NMVs; 1 mg) with RLP-Val (10 **mL**) via sonication for 20 **min** at 4 °C, followed by sequential extrusion from 400 to 200 nm, 10 times, using an Avanti mini extruder. The control formulation, NLP-Val, was synthesised in the same manner except that DSPE-SeSe-PEG2000 was substituted with its non-ROS-responsive counterpart, DSPE-PEG2000. **The encapsulated valsartan dose was kept consistent between the RLP-Val and NRLP-Val groups based on their respective encapsulation efficiency and drug loading capacity.**

2.3 Characterisation of NRLP-Val

The encapsulation efficiency of **valsartan** within NRLP-Val was quantified using high-performance liquid chromatography (HPLC). Chromatographic separation was achieved using a C18 column with an isocratic mobile phase consisting of methanol and deionised water (70:30, v/v) at a flow rate of 0.40 mL/min. **Valsartan** concentrations were determined using a standard curve. To evaluate the ROS-responsive release kinetics, NRLP-Val suspensions were aliquoted into six 1.5-mL centrifuge tubes. Each aliquot was incubated under one of three conditions: phosphate-buffered saline (PBS, pH 7.4), PBS containing 10 μM H_2O_2, or PBS containing 100 μM H_2O_2. Non-responsive NLP-Val nanoparticles served as controls. At predetermined time points (0, 1, 3, 6, and 12 h), tubes were centrifuged at 100,000 × g for 30 min. The pellet was collected and encapsulated **valsartan** was extracted using 500 μL of absolute ethanol. The amount of drug released was calculated using HPLC analysis of the extract relative to the total initial loading.

Subsequently, the morphology of NRLP-Val was examined using transmission electron microscopy (Tecnai G2 Spirit Twin, FEI) following a 12-h incubation in two distinct environments to assess structural stability: PBS (pH 7.4) and PBS containing 100 μM H_2O_2. Samples from each condition were negatively stained with 2% (w/v) sodium phosphotungstate solution (pH 7.0) for 60 s before imaging. Additionally, the hydrodynamic diameters and zeta potentials of the freshly prepared nanoparticles were measured in triplicate using dynamic light scattering (DLS; Zetasizer Nano ZS90, Malvern Instruments) with the samples dispersed in deionised water.

The protein profile of NRLP-Val was assessed using sodium dodecyl sulphate-polyacrylamide gel electrophoresis (SDS-PAGE). The nanoparticle protein (20 **μg**) was loaded onto a 10% polyacrylamide gel, electrophoresed, and stained with Coomassie Brilliant Blue R-250. Total protein quantification for equal loading was performed using a Rapid Coomassie Blue Assay Kit (Beyotime, China). The presence of specific neutrophil membrane proteins implicated in chemotaxis and adhesion was confirmed using western blotting. Proteins separated using SDS-PAGE were transferred onto polyvinylidene fluoride membranes. After blocking with 5% non-fat milk, the membrane was incubated overnight at 4 **°C** with the following primary antibodies (all from Abcam): rabbit anti-LFA-1 (ab13219), rabbit anti-CXCR2 (ab225732), rabbit anti-integrin α4 (ab75760), rabbit anti-integrin β1 (ab179472), and rabbit anti-Na^+/K^+-ATPase α1 (ab76020; loading control). Following three 10-min washes with TBST, the membrane was incubated with an HRP-conjugated goat anti-rabbit secondary antibody (Abcam) for 1 h at room temperature. Protein bands were visualised using an enhanced chemiluminescence substrate on a Bio-Rad Gel Doc™ XR+ System.

Finally, to verify the successful integration of NMVs with the synthetic lipid bilayer, a fluorescence labelling experiment was conducted. The lipid component was pre-labelled with the green fluorescent dye, DiD (1,1'-dioctadecyl-3,3,3',3'-tetramethylindodicarbocyanine perchlorate; Ex/Em: 644/665 nm; Invitrogen) and NMVs were labelled with the red fluorescent dye, DiO (3,3'-dioctadecyloxacarbocyanine perchlorate; Ex/Em: 484/501 nm; Sigma). Unincorporated dyes were removed via two cycles of centrifugation and washing. The labelled components were then fused by extrusion through a 200-nm polycarbonate membrane. The co-localisation of the DiO (red) and DiD (green) signals was assessed using a confocal laser scanning microscope (Leica TCS SP8) at 800× magnification.

2.4 Adult mouse cardiomyocyte (AMCM) isolation

AMCMs were isolated from 8 to 10-week-old C57BL/6J mice using a modified Langendorff-free enzymatic digestion protocol [35]. The mice were anaesthetised using an intraperitoneal injection of sodium pentobarbital (50 mg/kg). After a thoracotomy and full heart exposure, the descending aorta was transected. To prevent coagulation, 7 mL of ice-cold EDTA buffer (130 mM NaCl, 5 KCl, 0.5 mM $MgCl_2$, 10 mM HEPES, 10 mM glucose, 10 mM taurine, 5 mM pyruvate, 10 mM 2,3-butanedione monoxime, and 10 mM EDTA; pH 7.4) was rapidly injected into the right ventricle. The ascending aorta was clamped, and the heart was excised and transferred to a 6-cm dish containing EDTA buffer.

For enzymatic digestion, the heart was cannulated via the same left ventricular puncture site and sequentially perfused under gentle manual pressure with 10 mL of EDTA buffer, 3 mL of calcium-free perfusion buffer, and 50 mL of collagenase buffer (containing 1 mg/mL collagenase II, Worthington). Upon tissue softening, the heart was minced into approximately 1-mm^3 pieces and gently triturated using a wide-bore pipette. Digestion was terminated by adding 5 mL of stop buffer (perfusion buffer supplemented with 10% foetal bovine serum, FBS). The resulting cell suspension was filtered through a 100 **μm** nylon mesh. To ensure calcium tolerance, viable cardiomyocytes were purified through four rounds of gravity settling (5 **min** each) in a

series of buffers containing increasing calcium concentrations (0.1, 0.5, 1.0, and 1.8 mM).

Finally, the purified AMCMs were resuspended in pre-warmed Dulbecco's Modified Eagle Medium ((DMEM [Gibco], with 5% FBS, 10 mM BDM, and antibiotics) and plated at a density of 5×10^4 cells/cm² onto culture vessels pre-coated with laminin (5 **μg**/mL) for 1 h. After the initial attachment period, the plating medium was replaced with standard culture medium.

2.5 Cell lines and culture conditions

Human umbilical vein endothelial cells (HUVECs, ATCC® PCS-100-010™) and murine macrophage-like RAW 264.7 cells (ATCC® TIB-71™) were commercially procured. HUVECs were maintained in endothelial cell growth medium (ScienCell), and RAW 264.7 cells and attached AMCMs were cultured in high-glucose DMEM). All cultures were supplemented with 10% (v/v) heat-inactivated FBS, 100 U/mL penicillin, and 100 μg/mL streptomycin, and incubated at 37 **℃** in a humidified atmosphere containing 5% CO_2 .

2.6 In vitro binding analysis of NRLP-Val

HUVECs were plated in confocal dishes at a density of 1.5×10^5 cells per well and cultured for 24 h. To induce inflammation, the cells were stimulated with 10 ng/mL LPS for 10 h. Subsequently, the cells were incubated with 200 μL of DiD-labelled NRLP-Val or RLP-Val (X μg/mL) for 30 min at 37 °C. After uptake, the cells were washed, fixed with 4% paraformaldehyde (PFA) for 20 min, and blocked with 5% bovine serum albumin (BSA) for 1 h at room temperature. For immunofluorescence, samples were incubated with primary antibodies overnight at 4 °C, followed by the addition of appropriate secondary antibodies. Nuclei were counterstained with DAPI prior to imaging on an Olympus FV3000 confocal microscope.

2.7 Transwell assay

An in vitro transwell model (0.4 μm pore size, Millipore, USA) was established to simulate the injured cardiac microenvironment and evaluate the targeting efficiency of NRLP-Val. In this model, 1×10^5 HUVECs were seeded in the upper chamber and subjected to LPS stimulation. Subsequently, DiD-labelled RLP-Val and NRLP-Val nanoparticles were introduced. Following incubation, the media from both the upper and lower chambers were collected, and the fluorescence intensity was quantified using a microplate reader to assess nanoparticle translocation.

2.8 ATP assay

Cellular ATP levels were quantified using a firefly luciferase-based ATP assay kit (S0027; Beyotime) according to the manufacturer's protocol. Cells were lysed and centrifuged at 12,000 × g for 5 **min** at 4 **℃**. Subsequently, 20 μL of the supernatant was mixed with 100 μL of the detection reagent in a white opaque 96-well plate. After incubation for 5 **min** at room temperature, luminescence was measured using a microplate luminometer (BioTek Synergy2). ATP values were normalised to the total protein concentration.

2.9 Mitochondrial membrane potential and ROS measurements

Mitochondrial membrane potential (MMP) was evaluated using the fluorescent probe, JC-1 (C2003S, Beyotime). Cells were incubated with the JC-1 staining solution for 20 **min** at 37 **℃**, followed by washing and analysis. MMP was expressed as the ratio of red (aggregates) to green (monomers) fluorescence intensities. The mitochondrial superoxide production was measured using MitoSOX Red (M36008; Thermo Fisher Scientific). Cells were treated with 5 μM MitoSOX for 10 **min** at 37 **℃**, washed, and counterstained with Hoechst 33342 for nuclear visualisation. Fluorescence imaging and quantification were performed using the Operetta CLS High-Content Imaging System (Perkin Elmer).

2.10 Animals

Male C57 BL/6 and ICR mice were purchased from Shanghai Jiesijie Laboratory Animal Co., Ltd. All animal experiments were approved by the Ethics Committee of Zhongshan Hospital, Fudan University, Shanghai, China, and conducted in accordance with the guidelines for the Care and Use of Laboratory Animals published by the National Research Council (U.S.) Institute for Laboratory Animal Research (2024-249).

2.11 MI/R injury animal model

To establish a myocardial ischaemia/reperfusion (MI/R) model, the mice were anaesthetised and surgically prepared for left anterior descending (LAD) artery occlusion. Under isoflurane anaesthesia, the animals underwent tracheal intubation to facilitate positive-pressure ventilation. The surgical procedure involved a left thoracic incision to access the heart, allowing temporary ligation of the LAD using a 6-0 silk suture. The ligature was maintained for 60 **min** to induce regional ischaemia, after which it was released to allow reperfusion.

Successful induction of MI/R was confirmed using the characteristic ST-segment elevation observed on the electrocardiogram throughout the procedure.

2.12 Biodistribution and targeting specificity of NRLP-Val in vivo

To evaluate the biodistribution and cardiac targeting of the nanoparticles, mice undergoing MI/R surgery were randomly divided into two groups and received a single intravenous dose of DiD-labelled RLP-Val or NRLP-Val immediately after reperfusion (n=6 per group per time point). Biodistribution was assessed at four sequential time points: 2, 6, 12, and 24 h post-injection. At each terminal time point, the mice were euthanised, and their major organs (heart, liver, spleen, lung, kidney, and brain) were harvested for ex vivo fluorescence imaging using an in vivo imaging system (IVIS) (PerkinElmer). To further investigate cardiac targeting, additional heart samples collected at the 12-h mark were processed for immunofluorescence staining against cardiac troponin T (cTnT) and DAPI, with visualisation achieved through confocal microscopy. The local concentration of valsartan in the heart was quantified using HPLC.

2.13 Therapeutic effects of NRLP-Val in the acute phase of MI/R

To comprehensively evaluate the in vivo therapeutic effects of NRLP-Val during the acute phase of MI/R, a multimodal assessment was conducted 72 h post-treatment. The experimental workflow included small-animal PET-CTimaging, triphenyltetrazolium chloride (TTC) staining, dihydroethidium (DHE) staining, and TdT-mediated dUTP nick-end labelling (TUNEL) assay.

Mice were fasted for 12 h prior to PET imaging. Thirty minutes before the scan, 18F-FDG was administered via a tail vein injection. Myocardial metabolic activity was assessed by quantifying the cardiac 18F-FDG uptake using a dedicated small-animal PET system (model to be specified). Following the scan, the mice were euthanised and their hearts were harvested for subsequent histological analyses.

For infarct size quantification, the harvested hearts were sectioned perpendicular to the left ventricular long axis into 1-mm rings. The sections were incubated with 1% TTC in PBS at 37 **°C** for 25 **min**, followed by fixation with 4% PFA to terminate the reaction. The viable myocardium (stained red) and infarcted areas (pale white) were delineated and measured using the Image-Pro Plus 6.0 software.

To visualise ROS generation, cryosections (6 μm) were subjected to DHE staining. The sections were incubated with a DHE solution, yielding red fluorescence in the presence of superoxide, whereas the nuclei were counterstained blue with DAPI.

Apoptosis was detected in adjacent cryosections using a combined TUNEL and immunofluorescence protocol. After fixation with 4% PFA, permeabilisation, and blocking with 5% BSA, the sections were incubated overnight with a primary antibody against cTnT (Proteintech). This was followed by a 1-h incubation with an Alexa Fluor 488-conjugated secondary antibody at room temperature. The TUNEL reaction mixture was then applied to the sections and incubated at 37 **°C** for 1 h to label apoptotic nuclei. Finally, the sections were counterstained with DAPI. Fluorescent images were captured using an Olympus FV3000 confocal microscope and the number of TUNEL-positive nuclei within the cTnT-positive cardiomyocyte areas was quantified to determine the rate of cardiomyocyte-specific apoptosis..

2.14 Real time quantitative PCR (qPCR)

Total RNA was isolated from the heart tissue homogenates using a FastPure Cell/Tissue Total RNA Isolation Kit V2 (Vazyme Biotech Co. Ltd.). Subsequently, 500 ng of RNA from each sample was reverse transcribed into complementary DNA using a commercial reverse transcription reagent kit (TransGene). Gene expression levels were quantified using real-time quantitative PCR (qPCR) on a StepOnePlus Real-Time PCR System (Applied Biosystems) with the SYBR Green Master Mix. The specificity of each amplification was confirmed by observing a single peak in the melting curve. The primer sequences used were as follows: β-actin forward: 5′-GTGACGTTGACATCCGTAAAGA-3′; β-actin reverse: 5′-GCCGGACTCATCGTACTCC-3′; IL-1β forward: 5′-GAAATGCCACCTTTTGACAGTG-3′; IL-1β reverse: 5′-TGGATGCTCTCATCAGGACAG-3′; IL-6 forward: 5′-TAGTCCTTCCTACCCCAATTTCC-3′; IL-6 reverse: 5′-TTGGT CCTTAGCCACTCCTTC-3′; TNF-α forward: 5′-CCCTCACACTCAGATCATCTTCT-3′; TNF-α reverse: 5′-GCTACGACGTGGGCTACAG-3′.

2.15 Cardiac protection efficiency of NRLP-Val

At the 28-day endpoint following AMI, cardiac function was assessed using echocardiography (Visual Sonics Vevo 770)

under isoflurane anaesthesia. The left ventricular ejection fraction (LVEF) and left ventricular fractional shortening (LVFS) were calculated from two-dimensional M-mode traces. Subsequently, the hearts were excised and sectioned into 5–6-μm slices for histological analysis. The extent of fibrosis and infarct size were visualised and quantified using Masson's trichrome staining, whereas the cross-sectional area of the cardiomyocytes was evaluated using wheat germ agglutinin (WGA) staining.

2.16 Biosafety analysis of PLP- RvD1

To comprehensively evaluate the in vivo biosafety and immunomodulatory properties of NRLP-Val, healthy C57BL/6 mice were randomly assigned to receive either 200 μL of NRLP-Val (12 mg/kg) or an equal volume of PBS (n=6 per group). At predetermined time points after injection, the mice were euthanised for sample collection. The systemic inflammatory response was assessed by measuring IL-1β, IL-6, and TNF-α serum level using via ELISA. Coagulation function was profiled using citrate-anticoagulated whole blood, activated partial thromboplastin time (APTT) and prothrombin time (PT). Furthermore, potential organ toxicity was investigated by performing standard biochemical assays for liver function (AST and ALT) and renal function (CREA and UREA) on the collected serum, complemented by histopathological examination of the major organs via H&E staining.

2.17 Statistical analysis

All quantitative data are presented as the mean ± standard deviation. Statistical analyses were conducted using the GraphPad Prism software (version 8.2). For comparisons between the two groups, an unpaired two-tailed Student's t-test was used. When comparing three or more groups, a one-way analysis of variance was used, followed by Bonferroni's post-hoc test. A probability (P) value of less than 0.05 was considered statistically significant, with significance levels denoted as follows: $*P < 0.05$, $**P < 0.01$, and $***P < 0.001$.

3 Results and Discussion

3.1 Fabrication and characterisation of NRLP-Val

RLP-Val was constructed using a thin-film hydration method, in which ROS-responsive DSPE-Sese-PEG was added and valsartan was loaded during the hydration step (Fig. 1). Subsequently, NRLP-Val was formed by fusing NMVs with RLP-Val via serial extrusion. The size and zeta potential of RLP, RLP-Val, and NRLP-Val were measured using DLS on days 0, 1, 3, 5, and 7 (Fig. 2a–b). The size and zeta potential of all three formulations remained unchanged over 7 days, suggesting that these formulations are stable in PBS. On day 0, the average diameter increased from 135.98 ± 5.91 nm for RLP to 143.67 ± 6.01 nm for RLP-Val, which was close to that of NRLP-Val (146.33 ± 6.11 nm) (Fig. 2a). The mean zeta potential was -30.33 ± 4.93 mV for RLP-Val, similar to -31.89 ± 4.64 mV for RLP, which was neutralized to -22.97 ± 4.03 mV for NRLP-Val (Fig. 2b). The total membrane protein of NRLP-Val was determined using SDS-PAGE. The NMV protein profile was mostly preserved in NRLP-Val (Fig. 2e). Additionally, proteins associated with inflammatory cell tropism and chemotaxis, including lymphocyte function-associated antigen receptor (LFA-R), C-X-C motif chemokine receptor (CXCR2), **integrin α4**, and **integrin β1** were verified using western blotting (Fig. 2f). Furthermore, confocal images demonstrated the colocalization of NMV fluorescence (3,3′-dioctadecyloxacarbocyanine perchlorate, DiO) and RLP-Val (1,19-dioctadecyl-3,3,39,39-tetramethylindodicarbocyanine perchlorate, DiD-labelled lipid) after extrusion, in contrast to simple pipetting (Fig. 2j). These results indicated that NMV was successfully fused with RLP-Val. The encapsulation efficiency and drug loading capacity of NRLP-Val were assessed using HPLC. The results demonstrated that the encapsulation efficiency of NRLP-Val was 71.33% (Fig. 2c), and the drug loading capacity was 3.58% (Fig. 2d). Taken together, these data confirm the successful fabrication of stable, neutrophil membrane-cloaked nanoparticles with high drug loading and preservation of key membrane proteins essential for subsequent targeting.

3.2 ROS-responsive ability of NRLP-Val in vitro

We evaluated the cargo release capability of NRLP-Val in a high-ROS environment. After incubation with 100 μM H_2O_2 for 12 h, NRLP-Val lost its structural integrity and eventually became completely disassembled (Fig. 3a). Subsequently, NRLP-Val and NLP-Val were incubated in PBS and various concentrations of H_2O_2. The drug release profile indicated that in PBS, approximately 7.67% of valsartan was released from NRLP-Val after 12 h of incubation at 37 ℃ with shaking at 100 rpm. When NRLP-Val was incubated with 10 μM H_2O_2 for 12 **h**, the drug release rate increased to 52.17%. However, in the presence of 100 μM H_2O_2, the release of NRLP-Val was

explosive, reaching 80% within 1 h (Fig. 3b). The non-ROS-responsive control (NLP-Val) exhibited a minimal response under these conditions; specifically, valsartan release after 12 h did not exceed 10% at any concentration of H_2O_2. These results demonstrate that NRLP-Val can achieve the responsive release of valsartan in a high-ROS environment.

3.3 Targeting ability of NRLP-Val in vitro

We investigated whether NRLP-Val inherits the targeting ability of neutrophils in vitro. Immunofluorescence staining was performed to assess the binding capacity of NRLP-Val to HUVECs. Staining for intercellular adhesion molecule 1 (ICAM-1) demonstrated that NRLP-Val exhibited stronger binding to LPS-activated HUVECs than the RLP-Val control. To further elucidate the underlying mechanism, NRLP-Val was preincubated with an anti-LFA-1 antibody, considering the specific interaction between LFA-1 (on neutrophils) and ICAM-1 (Fig. 3c and 3e). This blockade resulted in a significant reduction in binding. Consistently. NRLP-Val specifically and efficiently targeted the vascular cell adhesion molecule 1 (VCAM-1) / very late antigen-4 (VLA-4) axis (Fig. 3d and 3f).

Next, we investigated the ability of NRLP-Val to traverse the Transwell model. HUVECs were cultured in the upper chamber and DiD-labelled NRLP-Val was introduced following LPS treatment (Fig. 3g). During construction of the transwell model, we confirmed 100% confluence of HUVECs using WGA staining (Fig. S1a). Compared with LPS treatment, lower fluorescence levels were detected in the lower chamber without LPS treatment. Despite the increased RLP-Val signals after LPS treatment, NRLP-Val exhibited significantly greater translocation across the endothelium (Fig. S1b). These findings indicate that NRLP-Val retains multi-ligand targeting and enhances the transendothelial migration capabilities of neutrophils through specific receptor-ligand interactions.

3.4 NRLP-Val crosses the endothelium via a transcytosis-independent pathway

The superior targeting capacity of NRLP-Val, mediated by multiple molecular partners, enhances its transendothelial migration. To elucidate the underlying mechanism, specifically, whether it occurs via the enhanced permeability and retention effect or transcytosis under inflamed conditions, we used a pharmacological inhibition approach. Pretreatment of HUVECs with dynasore (an endocytosis inhibitor) or bafilomycin A1 (an exocytosis inhibitor) did not significantly reduce NRLP-Val translocation, as quantified using flow cytometry (Fig. 4b). This finding was further corroborated using immunofluorescence analysis. In inflamed HUVECs, DiD-labelled NRLP-Val demonstrated minimal internalisation and poor co-localisation with lysosomes, and a significant association with the cytoskeleton, as labelled with WGA (Fig. 4a). Collectively, these data rule out transcytosis as the primary pathway, and support a paracellular route for NRLP-Val migration across the endothelial barrier.

3.5 NRLP-Val attenuates mitochondrial dysfunction and apoptosis in Ang II-stimulated cardiomyocytes in vitro

To evaluate the protective effect of NRLP-Val against mitochondrial dysfunction induced by local RAS activation, we stimulated primary AMCM with Ang II to establish an in vitro RAS activation model. Interventions were performed using either free valsartan or valsartan released from the ROS-responsive nanocarrier, NRLP-Val. MitoSOX fluorescence staining analysis revealed that valsartan released from NRLP-Val significantly inhibited Ang II-induced mitochondrial ROS generation, with an efficacy comparable to that of free valsartan (Fig. 4c and 4d). Further evaluation using the JC-1 probe to assess changes in mitochondrial membrane potential demonstrated that both forms of administration effectively restored membrane potential levels, with no statistically significant differences between the groups (Fig. 4e and 4f). Additionally, ATP production assays indicated that both valsartan released from NRLP-Val and free valsartan significantly increased the cellular ATP content (Fig. 4h). Collectively, these results demonstrated that in the Ang II-induced in vitro cardiomyocyte injury model, valsartan released by ROS-responsive NRLP-Val exhibited protective efficacy comparable to that of free valsartan in mitigating mitochondrial oxidative stress, membrane potential damage, and ATP production. To clarify, the protective effects of NRLP-Val on mitochondrial function, we evaluated the inhibitory effect of NRLP-Val on cardiomyocyte apoptosis using TUNEL staining. In the Ang II-induced apoptosis model, valsartan released by NRLP-Val exhibited an anti-apoptotic efficacy comparable to that of free valsartan (Fig. 4g). These in vitro results confirm that the ROS-responsive release from NRLP-Val does not compromise the bioactivity of valsartan in protecting cardiomyocytes against RAS activation-induced injury.

3.6 Biodistribution and targeting specificity of NRLP-Val in vivo

Subsequently, the targeting capability of NRLP-Val was evaluated using IVIS following intravenous administration. Owing to the incorporation of neutrophil membrane proteins, NRLP-Val exhibited significantly enhanced accumulation in the cardiac tissue compared to RLP-Val (Fig. 5a). Longitudinal live-animal imaging at 2, 6, 12, and 24 h after injection revealed a sustained higher fluorescence intensity of NRLP-Val in the heart than that of the control formulation (Fig. 5a and 5d). Notably, NRLP-Val also demonstrated a markedly lower fluorescence intensity in the liver than that of RLP-Val (Fig. 5e). Although both formulations underwent substantial clearance from major organs over time, NRLP-Val displayed significantly reduced hepatic retention, which could be attributed to its improved cardiac-targeting specificity (Fig. 5b). Quantitative analysis further corroborated the organ-specific distribution pattern, confirming the significantly lower hepatic accumulation of NRLP-Val than that of RLP-Val, without notable differences in other examined organs, thereby validating the enhanced targeting capacity and specificity of the biomimetic nanoparticle system (Fig. 5f–j). To further substantiate targeting efficacy, cardiac tissues were harvested and cryo-sectioned for microscopic examination. Confocal immunofluorescence imaging of myocardial sections demonstrated a substantially greater accumulation of DiD-labelled NRLP-Val than RLP-Val in the ischaemic border zone (Fig. 5c). Subsequent quantitative analysis using HPLC revealed a significantly higher local concentration of valsartan in the hearts of NRLP-Val-treated mice than that in RLP-Val- or free valsartan-treated mice (Fig. S2a). Collectively, these multifaceted analyses, including longitudinal in vivo imaging, ex vivo biodistribution, confocal microscopy of cardiac tissues, and quantitative assessment of local drug concentration, converge to unequivocally demonstrate the superior targeting efficacy of NRLP-Val.

3.7 Therapeutic effects of NRLP-Val in the acute phase of MI/R

For the in vivo efficacy study, 4 mg/kg of free valsartan was used. This dose was selected based on our previous studies, which confirmed that 4 mg/kg was the maximum safe dose for mice during the early acute phase[9, 36, 37]. Mice subjected to MI/R were randomly assigned to the PBS, Valsartan, RLP-Val, and NRLP-Val (4 mg/k), 8 mg/kg, or 12 mg/kg) groups to compare therapeutic effects (Fig. 6a).

We first assessed therapeutic efficacy by evaluating myocardial metabolic activity using PET imaging three days after reperfusion injury. No significant differences in metabolic activity were observed between the PBS, Valsartan, and RLP-Val groups. Notably, the myocardial metabolism was significantly higher in the 4 mg/kg NRLP-Val group than that in the RLP-Val group. Furthermore, both the 8 mg/kg and 12 mg/kg NRLP-Val groups exhibited enhanced metabolic activity relative to that of the 4 mg/kg NRLP-Val group, with no statistically significant differences between the two higher-dose groups (Fig. 6b and 6f). The infarct size was subsequently evaluated using TTC staining, which revealed no significant differences among the PBS, Valsartan, and RLP-Val groups. The 4 mg/kg NRLP-Val group demonstrated a significantly reduced infarct size compared with that of the RLP-Val group. Additionally, both the 8 mg/kg and 12 mg/kg NRLP-Val groups showed a further reduction in infarct size compared with that of the 4 mg/kg NRLP-Val group, with no significant difference between the two higher-dose groups (Fig. 6c and 6 g).

Moreover, NRLP-Val treatment mitigated oxidative stress in MI/R injury as assessed using DHE staining for ROS activity. Myocardial ROS levels were significantly lower in the 8 mg/kg NRLP-Val and 12 mg/kg NRLP-Val groups than that in the 4 mg/kg NRLP-Val group. The 4 mg/kg NRLP-Val group also exhibited reduced ROS levels compared with that in the PBS, Valsartan, and RLP-Val groups, with no significant differences among these groups (Fig. 6d and 6h). Collectively, the nanoparticle formulation effectively ameliorated mitochondrial dysfunction.

We further evaluated myocardial apoptosis using TUNEL staining. Both 8 mg/kg and 12 mg/kg NRLP-Val treatments significantly reduced cardiomyocyte apoptosis, demonstrating superior anti-apoptotic effects compared with that of 4 mg/kg NRLP-Val. The 4 mg/kg NRLP-Val group also showed significant apoptosis inhibition compared with that in the PBS, Valsartan, and RLP-Val groups, with no significant differences among the control groups (Fig. 6e and 6i). Furthermore, the expression levels of pro-inflammatory factors (IL-1β, IL-6, and TNF-α), measured using qPCR, were significantly lower in both the 8 mg/kg and 12 mg/kg NRLP-Val groups compared with that in the 4 mg/kg NRLP-Val group. The 4 mg/kg NRLP-Val group also exhibited reduced inflammatory cytokine levels compared with that of the PBS, Valsartan, and RLP-Val groups, with no

significant differences among the three control groups (Fig. S3a, S3b, and S3c). These findings demonstrated that valsartan was effectively released from NRLP-Val nanoparticles and exerted dose-dependent therapeutic effects across multiple parameters. The comparable efficacy observed between the 8 mg/kg and 12 mg/kg NRLP-Val groups in the early phase of acute myocardial infarction suggests that the 8 mg/kg dose may represent an optimal and potentially translatable regimen for clinical development.

3.8 Therapeutic effects of NRLP-Val on heart remodelling

We evaluated the long-term cardioprotective effects of intravenous administration over 28 days following MI/R injury using WGA staining, Masson's trichrome staining, and echocardiography across the following treatment groups: PBS, Valsartan, RLP-Val, and NRLP-Val (4 mg/kg, 8 mg/kg, and 12 mg/kg).

WGA staining revealed a significant reduction in the cardiomyocyte cross-sectional area in the 4 mg/kg NRLP-Val group compared with that in the PBS, Valsartan, and RLP-Val groups, among which no significant differences were observed. Further reductions in the cross-sectional area were noted in both the 8 mg/kg and 12 mg/kg NRLP-Val groups compared with that in the 4 mg/kg NRLP-Val group, with no statistically significant difference between the two higher-dose groups (Fig. 7a and 7c).

Masson's trichrome staining demonstrated that myocardial fibrosis was significantly attenuated in the NRLP-4 mg/kg Val group, accompanied by a thicker infarct wall than that in the PBS, Valsartan, and RLP-Val groups. Enhanced antifibrotic and structural protective effects were observed in the 8 mg/kg and 12 mg/kg NRLP-Val groups, which exhibited further reductions in fibrosis and improved wall thickness compared with those in the 4 mg/kg NRLP-Val group, with no significant differences between the two higher-dose regimens. No notable differences were detected between the PBS, Valsartan, and RLP-Val groups (Fig. 7b, 7d, and 7e).

Echocardiographic assessment indicated that LVEF and LVFS were significantly improved in the 4 mg/kg NRLP-Val group compared with those in the PBS, Valsartan, and RLP-Val groups. Further enhancements in cardiac function were noted in the 8 mg/kg and 12 mg/kg NRLP-Val groups, which exhibited higher LVEF and LVFS than those in the 4 mg/kg NRLP-Val group, with no significant differences between the two higher doses. Additionally, ventricular remodelling was ameliorated in the 8 mg/kg and 12 mg/kg NRLP-Val groups, as evidenced by the reduced left ventricular end-diastolic volume and left ventricular end-systolic volume compared with those in the 4 mg/kg NRLP-Val group. The 4 mg/kg NRLP-Val group also showed improved ventricular volumes compared with those in the PBS, Valsartan, and RLP-Val groups, among which no significant differences were detected (Fig. 7f, 7g, 7h, and 7i).

These long-term efficacy results demonstrated that NRLP-Val confers significant functional and structural improvements compared to RLP-Val and free valsartan, with a dose-dependent efficacy of up to 8 mg/kg. Given the comparable therapeutic benefits of 8 mg/kg and 12 mg/kg NRLP-Val, the 8 mg/kg dose was identified as a promising candidate for further clinical translation.

3.9 Biosafety assessment of NRLP-Val

To assess the biosafety of NRLP-Val, we evaluated a series of safety parameters in healthy mice treated with PBS or 12 mg/kg NRLP-Val. Serum levels of the pro-inflammatory cytokines **IL-1β,** IL-6, and **TNF-α**, quantified using ELISA three days after treatment, showed no significant differences between the 12 mg/kg NRLP-Val and PBS groups, indicating the absence of systemic inflammation (Fig. 8a). Coagulation profiles, including the APTT and PT, were also unaffected by NRLP-Val administration (Fig. 8b). Furthermore, biochemical analysis revealed no notable changes in the markers of hepatic injury (ALT and AST) or renal function (CREA and UREA), suggesting a lack of liver or kidney toxicity (Fig. 8b and 8c). Collectively, these results confirmed the favourable biosafety profile of NRLP-Val, even at a high dose of 12 mg/kg, supporting its potential for further therapeutic development. It is reasonable to assume that lower doses (4 and 8 mg/kg) exhibited similar safety characteristics.

4 Conclusion

We successfully developed NRLP-Val, a neutrophil membrane-biomimetic and ROS-responsive nanoparticle designed for the targeted and on-demand delivery of valsartan to the infarcted heart. This integrated platform exhibited superior cardiac targeting, site-specific drug release, and significant multimodal protection against ischaemia/reperfusion injury. By effectively decoupling potent local RAS inhibition from systemic side effects, NRLP-Val addresses the fundamental limitations of current pharmacotherapy and is a promising candidate for enhancing outcomes following AMI. This study established a versatile bio-inspired strategy for the precise treatment of other

inflammatory diseases.

Electronic Supplementary Material: Supplementary material (please provide the brief detail of the ESM) is available in the online version of this article at https://doi.org/10.26599/NR.2026.94908732.

Data availability

All data to support the conclusions of this paper are presented in the manuscript and/or Electronic Supplementary Material. Additional data related to this study can be obtained from the corresponding author upon request.

Acknowledgements

The authors thank the Shiyanjia Lab (www.shiyanjia.com) for the transmission electron microscopy measurements. The authors are grateful to Ms. Xiao Guo at the Joint Live Small Animal Imaging Laboratory of Fudan University Shanghai Medical College-PerkinElmer Company for the technical support with the in vivo imaging system. This work was financially supported by the Xinjiang Uygur Autonomous Region Natural Science Foundation (2024D01C279), Kashi Prefecture Science and Technology Plan (KS2024023), and (82400532, 82570495, 82200449, and 82300479).

Declaration of competing interest

The authors declare that they have no competing financial interests or personal relationships that may have influenced the work reported in this study.

Author contribution statement

Author Wusiman Yakufu, Yuekai Shi, and Jinfeng Gao contributed equally to this work including project build, paper writing, and every part of the paper. Ayitongguli Aimaiti, Nueraili Kadi, Qiyu Li, Miribanguli Alifu and Zhenzhen Huang contributed to data analysis. Muhetaer Wubuli, Reyimai Mutailipu, Abulimiti Jamali, Aikebaier Yasen and Wumaierjiang Kelimu contributed to data collection. Yang Pang, Su Li, Rongrong Lu and Maimaitiaili Tuerxun constructed the animal models. Qibing Wang, Xianglin Tang, and Junbo Ge provided experimental platforms. Yuqiong Chen, Abudureheman Mijiti and Zheyong Huang supervised the project. All authors read and approved the final manuscript.

Informed consent

Not applicable

Ethics statement

All experimental procedures were conducted in accordance with the institutional guidelines for the care and use of laboratory animals, and protocols, which were approved by the Animal Care and Use Committee of Zhongshan Hospital, Shanghai, People's Republic of China (2024-249).

Use of AI statement

None

References

[1] Global, regional, and national age-sex specific mortality for 264 causes of death, 1980-2016: a systematic analysis for the Global Burden of Disease Study 2016. *Lancet (London, England)* **2017**, *390*, 1151-1210.

[2] Heusch, G. Myocardial ischaemia-reperfusion injury and cardioprotection in perspective. *Nat Rev Cardiol* **2020**, *17*, 773-789.

[3] Gershlick, A. H.;Banning, A. P.;Myat, A.;Verheugt, F. W.; Gersh, B. J. Reperfusion therapy for STEMI: is there still a role for thrombolysis in the era of primary percutaneous coronary intervention? *Lancet (London, England)* **2013**, *382*, 624-632.

[4] Khan, M. S.;Shahid, I.;Bennis, A.;Rakisheva, A.;Metra, M.; Butler, J. Global epidemiology of heart failure. *Nat Rev Cardiol* **2024**, *21*, 717-734.

[5] Yamagishi, H.;Kim, S.;Nishikimi, T.;Takeuchi, K.; Takeda, T. Contribution of cardiac renin-angiotensin system to ventricular remodelling in myocardial-infarcted rats. *J Mol Cell Cardiol* **1993**, *25*, 1369-1380.

[6] Oyamada, S.;Bianchi, C.;Takai, S.;Robich, M. P.;Clements, R. T.;Chu, L.; Sellke, F. W. Impact of acute myocardial ischemia reperfusion on the tissue and blood-borne renin-angiotensin system. *Basic Res Cardiol* **2010**, *105*, 513-522.

[7] Kumar, R.;Singh, V. P.; Baker, K. M. The intracellular renin-angiotensin system in the heart. *Current hypertension reports* **2009**, *11*, 104-110.

[8] Sun, Y. Intracardiac renin-angiotensin system and myocardial repair/remodeling following infarction. *J Mol Cell Cardiol* **2010**, *48*, 483-489.

[9] Gao, J.;**Yakufu, W.**;Yang, H.;Song, Y.;Wang, Q.;Li, Q.;Tan, H.;Chen, J.;Sun, D.;Wang, Z.;Zhang, J.;Weng, X.;Qian, J.;Pang, Z.;Wang, Q.;Huang, Z.; Ge, J. Early initiation of ARBs without blood pressure risk via neutrophil membrane-fused pH-sensitive liposomes to reduce cardiomyocyte apoptosis after acute myocardial infarction. *Nano Research* **2023**, 10.1007/s12274-023-5846-0.

[10] Becari, C.;Silva, M. A. B.;Durand, M. T.;Prado, C. M.;Oliveira, E. B.;Ribeiro, M. S.;Salgado, H. C.;Salgado, M. C. O.; Tostes, R. C. Elastase-2, an angiotensin II-generating enzyme, contributes to increased angiotensin II in resistance arteries of mice with myocardial infarction. *Br J Pharmacol* **2017**, *174*, 1104-1115.

[11] Forrester, S. J.;Booz, G. W.;Sigmund, C. D.;Coffman, T. M.;Kawai, T.;Rizzo, V.;Scalia, R.; Eguchi, S. Angiotensin II Signal Transduction: An Update on Mechanisms of Physiology and Pathophysiology. *Physiol Rev* **2018**, *98*, 1627-1738.

[12] de Cavanagh, E. M.;Inserra, F.; Ferder, L. Angiotensin II blockade: a strategy to slow ageing by protecting mitochondria? *Cardiovasc Res* **2011**, *89*, 31-40.

[13] Xu, J.;Carretero, O. A.;Liao, T. D.;Peng, H.;Shesely, E. G.;Xu, J.;Liu, T. S.;Yang, J. J.;Reudelhuber, T. L.; Yang, X. P. Local angiotensin II aggravates cardiac remodeling in hypertension. *Am J Physiol Heart Circ Physiol* **2010**, *299*, H1328-1338.

[14] Danser, A. H. Cardiac angiotensin II: does it have a function? *Am J Physiol Heart Circ Physiol* **2010**, *299*, H1304-1306.

[15] Ferrario, C. M. Cardiac remodelling and RAS inhibition. *Ther Adv Cardiovasc Dis* **2016**, *10*, 162-171.

[16] Jugdutt, B. I.;Jelani, A.;Palaniyappan, A.;Idikio, H.;Uweira, R. E.;Menon, V.; Jugdutt, C. E. Aging-related early changes in markers of ventricular and matrix remodeling after reperfused ST-segment elevation myocardial infarction in the canine model: effect of early therapy with an angiotensin II type 1 receptor blocker. *Circulation* **2010**, *122*, 341-351.

[17] Rao, S. V.;O'Donoghue, M. L.;Ruel, M.;Rab, T.;Tamis-Holland, J. E.;Alexander, J. H.;Baber, U.;Baker, H.;Cohen, M. G.;Cruz-Ruiz, M.;Davis, L. L.;de Lemos, J. A.;DeWald, T. A.;Elgendy, I. Y.;Feldman, D. N.;Goyal, A.;Isiadinso, I.;Menon, V.;Morrow, D. A.;Mukherjee, D.;Platz, E.;Promes, S. B.;Sandner, S.;Sandoval, Y.;Schunder, R.;Shah, B.;Stopyra, J. P.;Talbot, A. W.;Taub, P. R.; Williams, M. S. 2025 ACC/AHA/ACEP/NAEMSP/SCAI Guideline for the Management of Patients With Acute Coronary Syndromes: A Report of the American College of Cardiology/American Heart Association Joint Committee on Clinical Practice Guidelines. *Circulation* **2025**, *151*, e771-e862.

[18] Byrne, R. A.;Rossello, X.;Coughlan, J. J.;Barbato, E.;Berry, C.;Chieffo, A.;Claeys, M. J.;Dan, G. A.;Dweck, M. R.;Galbraith, M.;Gilard, M.;Hinterbuchner, L.;Jankowska, E. A.;Jüni, P.;Kimura, T.;Kunadian, V.;Leosdottir, M.;Lorusso, R.;Pedretti, R. F. E.;Rigopoulos, A. G.;Rubini Gimenez, M.;Thiele, H.;Vranckx, P.;Wassmann, S.;Wenger, N. K.; Ibanez, B. 2023 ESC Guidelines for the management of acute coronary syndromes. *Eur Heart J* **2023**, *44*, 3720-3826.

[19] Tan, H.;Li, W.;Pang, Z.;Weng, X.;Gao, J.;Chen, J.;Wang, Q.;Li, Q.;Yang, H.;Dong, Z.;Wang, Z.;Zhu, G.;Tan, Y.;Fu, Y.;Han, C.;Cai, S.;Qian, J.;Huang, Z.;Song, Y.; Ge, J. Genetically Engineered Macrophages Co‐Loaded with CD47 Inhibitors

Synergistically Reconstruct Efferocytosis and Improve Cardiac Remodeling Post Myocardial Ischemia Reperfusion Injury. *Advanced Healthcare Materials* **2024**, *13*.

[20] Zhang, N.;Fan, M.;Zhao, Y.;Hu, X.;Zhu, Q.;Jiao, X.;Lv, Q.;Li, D.;Huang, Z.;Fu, G.;Ge, J.;Li, H.; Zhang, W. Biomimetic and NOS‐Responsive Nanomotor Deeply Delivery a Combination of MSC‐EV and Mitochondrial ROS Scavenger and Promote Heart Repair and Regeneration. *Advanced Science* **2023**, *10*.

[21] Yu, H.;Jin, F.;Liu, D.;Shu, G.;Wang, X.;Qi, J.;Sun, M.;Yang, P.;Jiang, S.;Ying, X.; Du, Y. ROS-responsive nano-drug delivery system combining mitochondria-targeting ceria nanoparticles with atorvastatin for acute kidney injury. *Theranostics* **2020**, *10*, 2342-2357.

[22] Liu, G.;Zhao, X.;Zhang, Y.;Xu, J.;Xu, J.;Li, Y.;Min, H.;Shi, J.;Zhao, Y.;Wei, J.;Wang, J.; Nie, G. Engineering Biomimetic Platesomes for pH-Responsive Drug Delivery and Enhanced Antitumor Activity. *Adv Mater* **2019**, *31*, e1900795.

[23] Gao, J.;Pang, Z.;Wang, Q.;Tan, Y.;Li, Q.;Tan, H.;Chen, J.;Yakufu, W.;Wang, Z.;Yang, H.;Zhang, J.;Sun, D.;Weng, X.;Wang, Q.;Qian, J.;Song, Y.;Huang, Z.; Ge, J. Biomimetic Nano-Degrader Based CD47-SIRPα Immune Checkpoint Inhibition Promotes Macrophage Efferocytosis for Cardiac Repair. *Adv Sci (Weinh)* **2024**, 10.1002/advs.202306388, e2306388.

[24] Tan, H.;Song, Y.;Chen, J.;Zhang, N.;Wang, Q.;Li, Q.;Gao, J.;Yang, H.;Dong, Z.;Weng, X.;Wang, Z.;Sun, D.;Yakufu, W.;Pang, Z.;Huang, Z.; Ge, J. Platelet-Like Fusogenic Liposome-Mediated Targeting Delivery of miR-21 Improves Myocardial Remodeling by Reprogramming Macrophages Post Myocardial Ischemia-Reperfusion Injury. *Adv Sci (Weinh)* **2021**, *8*, e2100787.

[25] Zhang, N.;Song, Y.;Huang, Z.;Chen, J.;Tan, H.;Yang, H.;Fan, M.;Li, Q.;Wang, Q.;Gao, J.;Pang, Z.;Qian, J.; Ge, J. Monocyte mimics improve mesenchymal stem cell-derived extracellular vesicle homing in a mouse MI/RI model. *Biomaterials* **2020**, *255*, 120168.

[26] Cai, S.;Gao, J.;Weng, X.;Wang, Z.;Zheng, D.;Wang, Q.;Li, Q.;Han, C.;Li, W.;Chen, J.;Fu, Y.;Tan, Y.;Wei, B.;Pang, Z.;Huang, Z.;Song, Y.; Ge, J. Synergistic enhancement of efferocytosis and cholesterol efflux via macrophage biomimetic nanoparticle to attenuate atherosclerosis progression. *Bioact Mater* **2026**, *55*, 131-143.

[27] Fang, R. H.;Kroll, A. V.;Gao, W.; Zhang, L. Cell Membrane Coating Nanotechnology. *Adv Mater* **2018**, *30*, e1706759.

[28] Li, M.;Guo, Q.;Zhong, C.; Zhang, Z. Multifunctional cell membranes-based nano-carriers for targeted therapies: a review of recent trends and future perspective. *Drug delivery* **2023**, *30*, 2288797.

[29] Fang, R. H.;Gao, W.; Zhang, L. Targeting drugs to tumours using cell membrane-coated nanoparticles. *Nature reviews. Clinical oncology* **2023**, *20*, 33-48.

[30] Pell, V. R.;Chouchani, E. T.;Murphy, M. P.;Brookes, P. S.; Krieg, T. Moving Forwards by Blocking Back-Flow: The Yin and Yang of MI Therapy. *Circ Res* **2016**, *118*, 898-906.

[31] Bugger, H.; Pfeil, K. Mitochondrial ROS in myocardial ischemia reperfusion and remodeling. *Biochimica et biophysica acta. Molecular basis of disease* **2020**, *1866*, 165768.

[32] González-Montero, J.;Brito, R.;Gajardo, A. I.; Rodrigo, R. Myocardial reperfusion injury and oxidative stress: Therapeutic opportunities. *World journal of cardiology* **2018**, *10*, 74-86.

[33] Mosca, T.; Forte, W. C. Comparative Efficiency and Impact on the Activity of Blood Neutrophils Isolated by Percoll, Ficoll and Spontaneous Sedimentation Methods. *Immunol Invest* **2016**, *45*, 29-37.

[34] He, Y.;Li, R.;Li, H.;Zhang, S.;Dai, W.;Wu, Q.;Jiang, L.;Zheng, Z.;Shen, S.;Chen, X.;Zhu, Y.;Wang, J.; Pang, Z. Erythroliposomes: Integrated Hybrid Nanovesicles Composed of Erythrocyte Membranes and Artificial Lipid Membranes for Pore-Forming Toxin Clearance. *ACS Nano* **2019**, *13*, 4148-4159.

[35] Ackers-Johnson, M.;Li, P. Y.;Holmes, A. P.;O'Brien, S. M.;Pavlovic, D.; Foo, R. S. A Simplified, Langendorff-Free Method for Concomitant Isolation of Viable Cardiac Myocytes and Nonmyocytes From the Adult Mouse Heart. *Circ Res* **2016**, *119*, 909-920.

[36] Suematsu, Y.;Miura, S.;Goto, M.;Matsuo, Y.;Arimura, T.;Kuwano, T.;Imaizumi, S.;Iwata, A.;Yahiro, E.; Saku, K. LCZ696, an angiotensin receptor-neprilysin inhibitor, improves cardiac function with the attenuation of fibrosis in heart failure with reduced ejection fraction in streptozotocin-induced diabetic mice. *Eur J Heart Fail* **2016**, *18*, 386-393.

[37] Torrado, J.;Cain, C.;Mauro, A. G.;Romeo, F.;Ockaili, R.;Chau, V. Q.;Nestler, J. A.;Devarakonda, T.;Ghosh, S.;Das, A.; Salloum, F. N. Sacubitril/Valsartan Averts Adverse Post-Infarction Ventricular Remodeling and Preserves Systolic Function in Rabbits. *J Am Coll Cardiol* **2018**, *72*, 2342-2356.

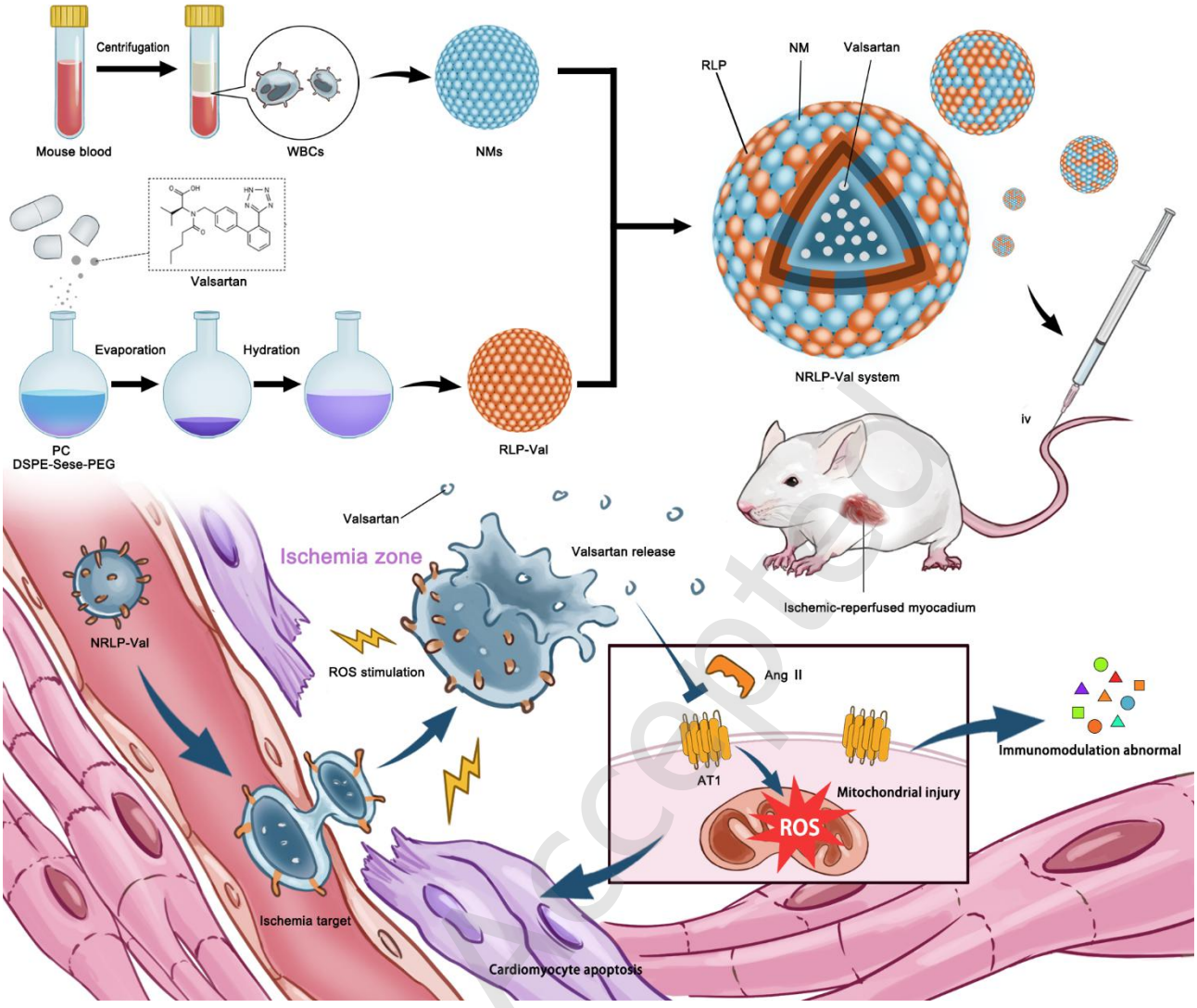

Figure 1. Schematic illustration of the fabrication of NRLP-Val and its mechanism for targeted therapy of myocardial ischemia/reperfusion injury. NRLP-Val was constructed by fusing neutrophil membrane vesicles with a reactive oxygen species (ROS)-responsive lipid nanoparticle core loaded with valsartan. This biomimetic nanocarrier preferentially accumulates in ischemic myocardium and releases valsartan in response to the elevated ROS microenvironment, thereby selectively inhibiting the local renin–angiotensin system to ameliorate MI/R injury.

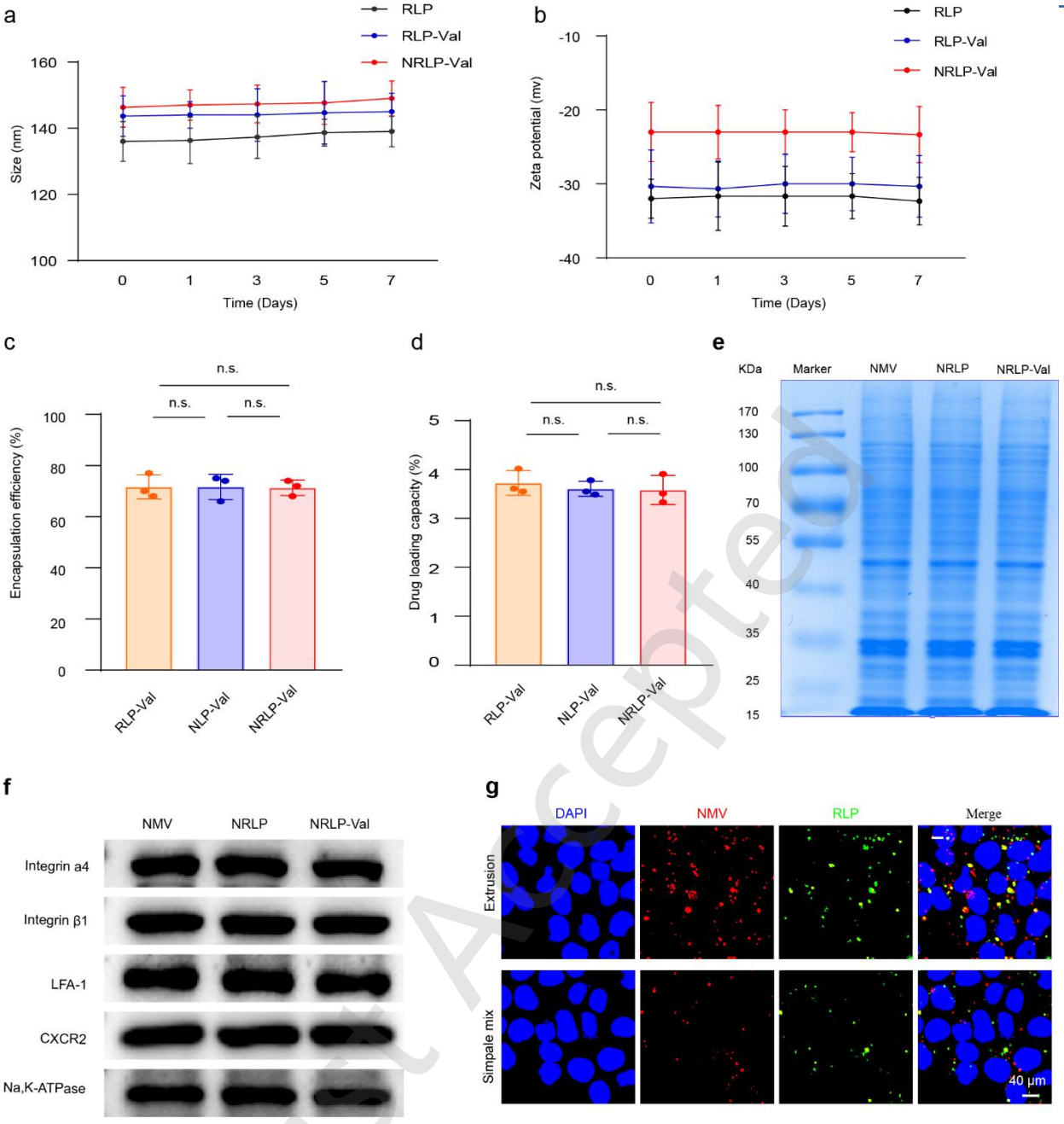

Figure 2. Characterization of NRLP-Val. (a) Size of RLP, RLP-Val, and NRLP-Val measured by dynamic light scattering (DLS) over 7 days(n=3). (b) Zeta potential of RLP, RLP-Val, and NRLP-Val measured by DLS over 7 days(n=3). (c) Encapsulation efficiency of NRLP-Val quantified by HPLC. (d) Drug loading capacity of NRLP-Val quantified by HPLC. (e) SDS–PAGE analysis of NMV, NRLP, and NRLP-Val. (f) Western blot analysis of key neutrophil membrane proteins (LFA-R, CXCR2, integrin α4, and integrin β1) in NMV and NRLP-Val. (g) CLSM images of extruded NMV (red) and RLP-Val (green) after incubation with Raw264.7 cells for 20 min, demonstrating successful membrane fusion.

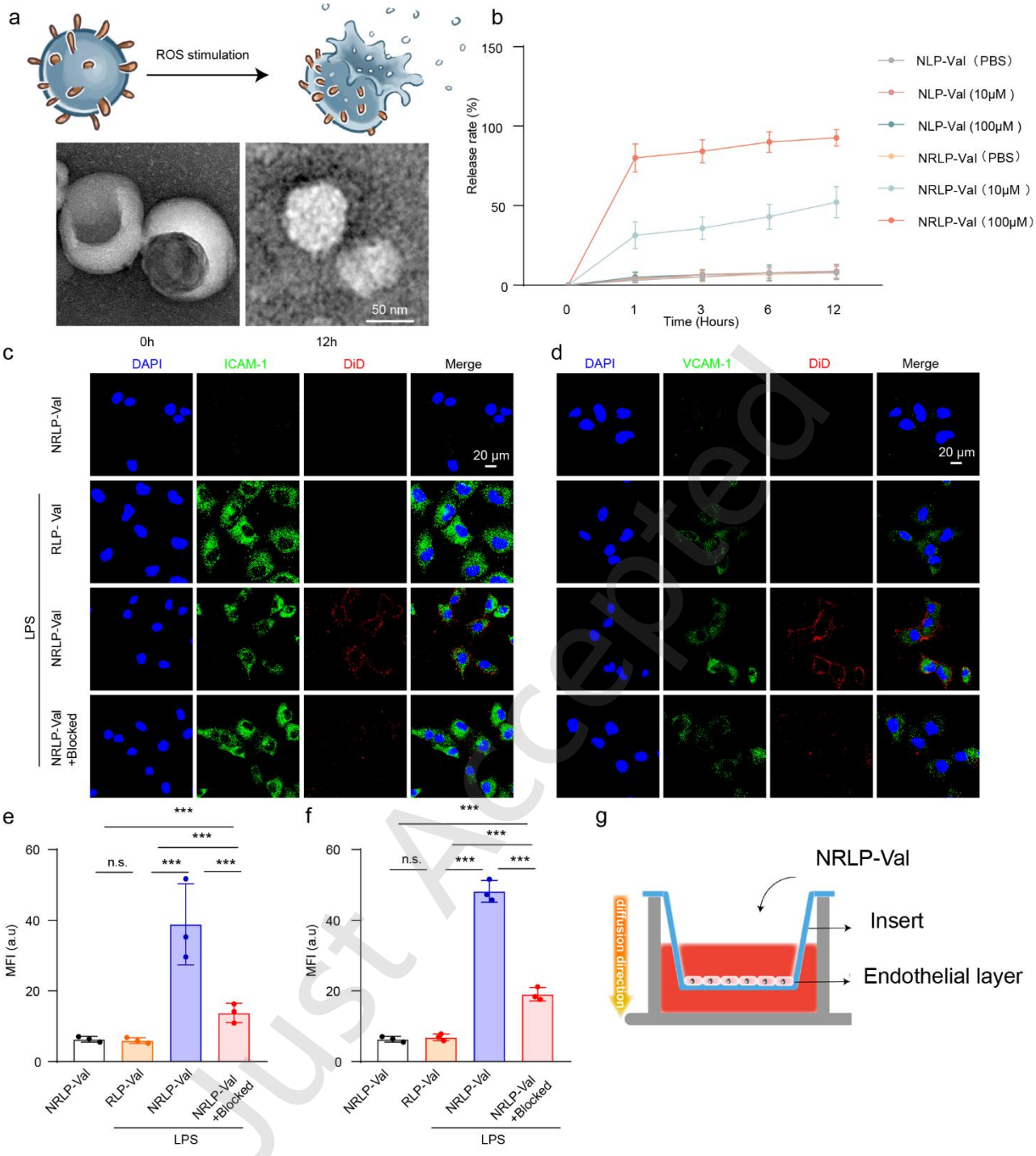

Figure 3. ROS-responsive drug release and in vitro targeting ability of NRLP-Val.(a) The inset illustrates the ROS-triggered disassembly of NRLP-Val and transmission electron microscopy (TEM) images showing the structural disintegration of NRLP-Val after 12 h incubation in 100 μM H_2O_2. (b) Cumulative release profile of valsartan from NRLP-Val and the non-ROS-responsive control (NLP-Val) under PBS and different H_2O_2 concentrations (10, 100 μM). (c) The binding of RLP-Val, NRLP-Val, and anti-LAF-1-blocked NSLP-Val to LPS-pretreated (or untreated) HUVECs was imaged after staining for ICAM-1 (green), with (e) quantitative assays. (d)The binding of RLP-Val, NRLP-Val, and anti-VLA-4-blocked NRLP-Val to LPSpretreated (or untreated) HUVECs was imaged after staining for VCAM-1(green), with (f) quantitative assays(n=3). (g) Schematic diagram of the transwell permeability model. Results are presented as the mean ± SD. n.s. indicates not significant, ***P < 0.001.

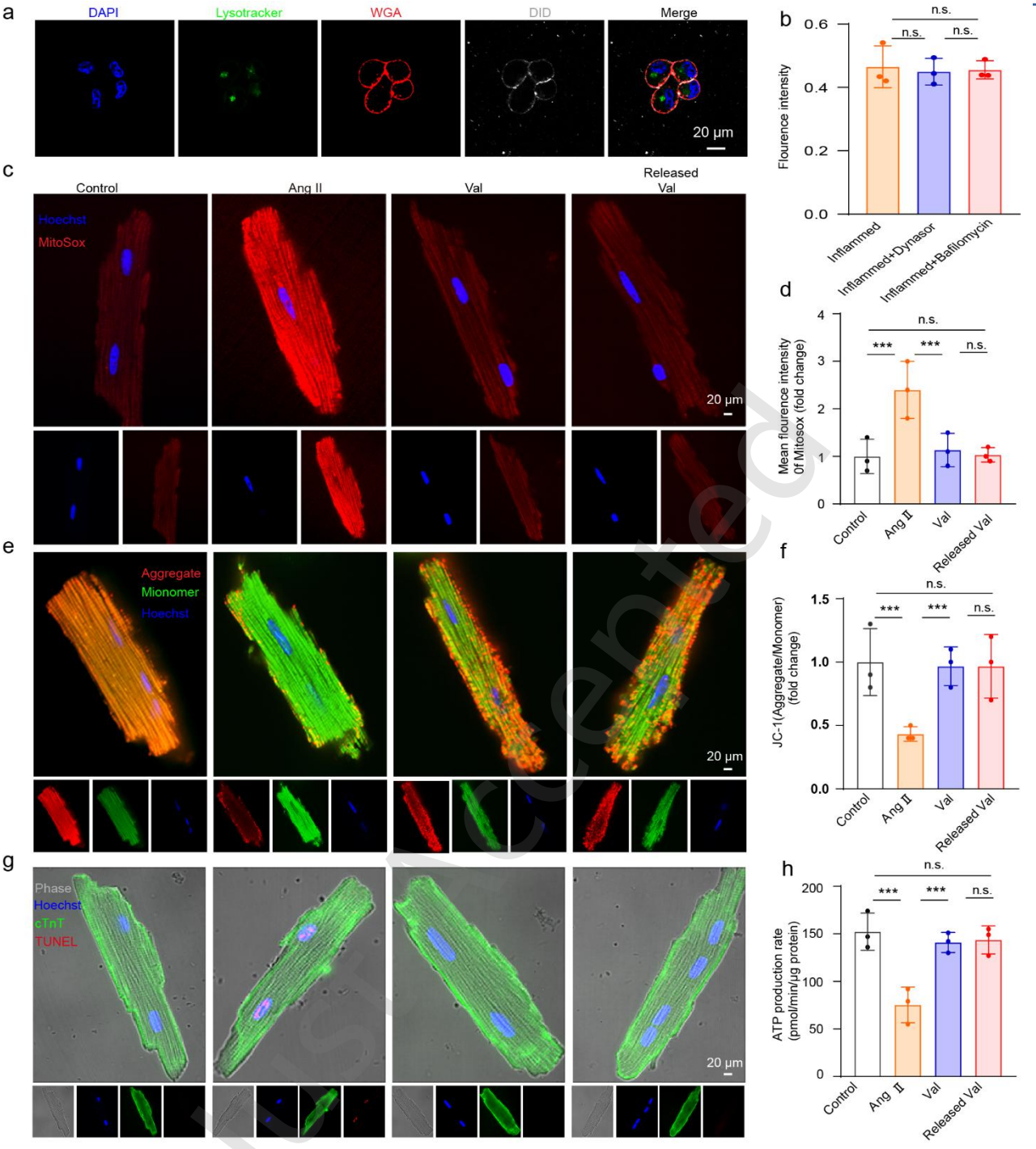

Figure 4. Mechanism of NRLP-Val endothelial translocation and its protective effects against mitochondrial dysfunction and apoptosis in vitro. (a) Representative confocal images of LPS-activated HUVECs incubated with DiD-labeled NRLP-Val (white). Cells were co-stained for lysosomes (LAMP-1, green) and cytoskeleton (WGA, red). (b) Flow cytometric quantification of fluorescence intensity in the lower chamber of a transwell system 1 h after adding NRLP-Val to HUVEC monolayers pretreated with PBS, dynasore (endocytosis inhibitor), or bafilomycin (exocytosis inhibitor) (n = 3). (C, D) Representative MitoSOX staining images (c) and quantification of mitochondrial superoxide fluorescence intensity (d) in primary adult mouse cardiomyocytes (AMCMs) treated with Ang II, free valsartan (Val), or valsartan released from NRLP-Val (Released Val) (n=10). (e, f) Representative JC-1 staining images (e) and quantification of red/green fluorescence ratio reflecting mitochondrial membrane potential (f) in AMCMs under the indicated treatments (n=10). (g) Representative TUNEL staining images of AMCMs showing apoptotic nuclei (green). (h) Cellular ATP content measured by a bioluminescence assay. Results are presented as the mean ± SD. n.s. indicates not significant, $P > 0.05$, *$P < 0.05$, **$P < 0.01$, ***$P < 0.001$.

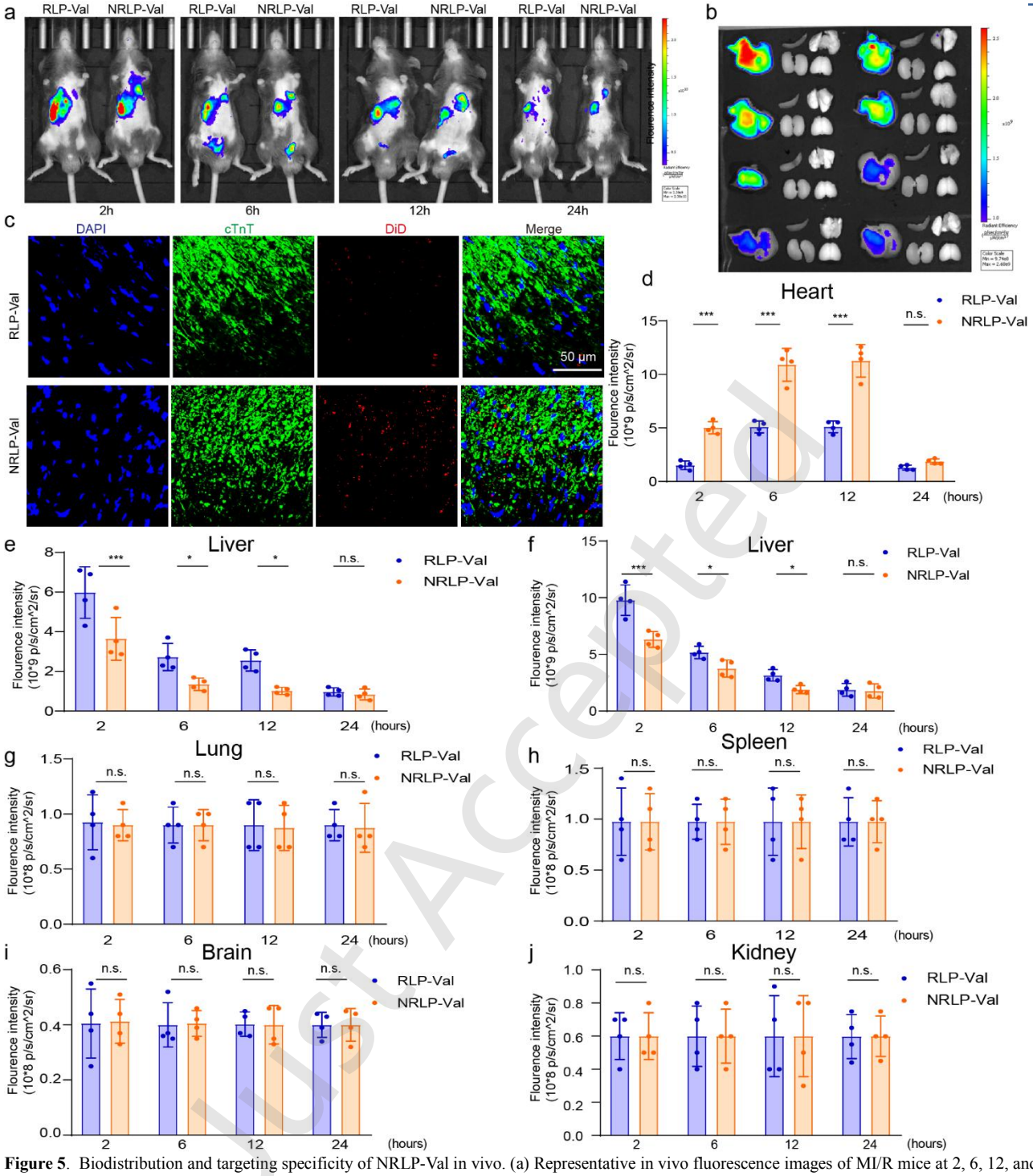

Figure 5. Biodistribution and targeting specificity of NRLP-Val in vivo. (a) Representative in vivo fluorescence images of MI/R mice at 2, 6, 12, and 24 h after intravenous injection of DiD-labeled RLP-Val l or NRLP-Val. (b) Corresponding ex vivo fluorescence images of major organs (liver, lung, spleen, brain, kidney) at 2, 6, 12, and 24 h after intravenous injection of DiD-labeled RLP-Val or NRLP-Val. (c) Immunofluorescence images of heart sections showing the targeted accumulation of RLP-Val and NRLP-Val after staining for cTnT. (d, e) Time-course quantification of cardiac and hepatic signals from in vivo imaging in (a). (f–j) Ex vivo fluorescence intensities of the liver, lung, spleen, brain and kidney from (b) (n=4). Results are presented as the mean ± SD. n.s. indicates not significant, $P > 0.05$, *$P < 0.05$, **$P < 0.01$, ***$P < 0.001$.

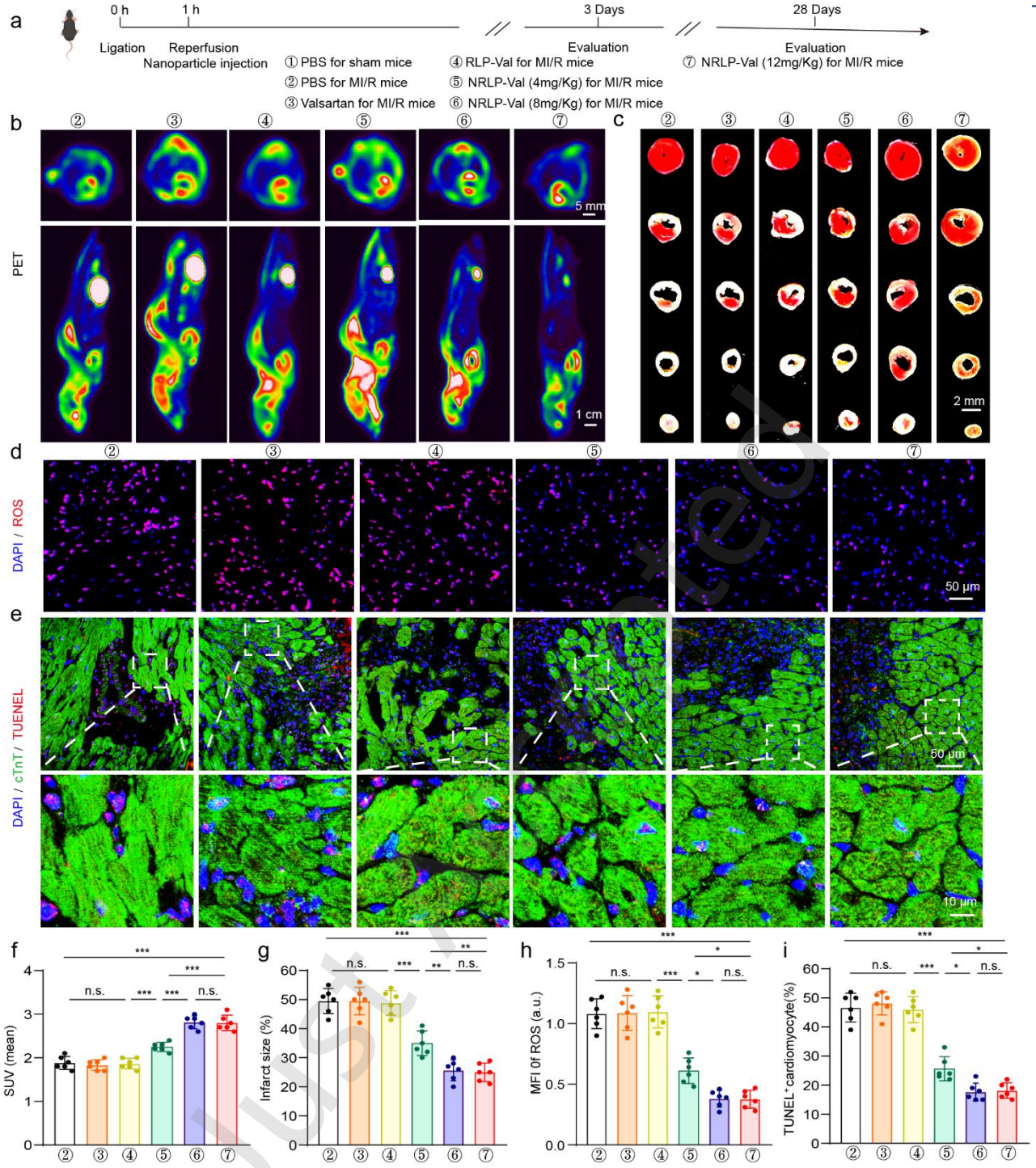

Figure 6. Therapeutic efficacy of NRLP-Val in the acute phase of myocardial ischemia/reperfusion (MI/R) injury. (a) Schematic timeline of the experimental design for in vivo therapeutic evaluation. (b) Representative myocardial ^{18} F-FDG micro-PET images and (f) quantitative analysis of standardized uptake value (SUV mean) at 3 days post-MI/R, reflecting myocardial metabolic activity. (c) Representative triphenyltetrazolium chloride (TTC)-stained heart sections and (g) quantification of infarct size. (d) Representative dihydroethidium (DHE) staining images and (h) quantitative analysis of reactive oxygen species (ROS) levels in myocardial sections. (e) Representative TUNEL staining images of the border zone and (i) quantification of apoptotic cardiomyocytes. Mice were treated with PBS, free Valsartan, RLP-Val, or NRLP-Val at doses of 4, 8, and 12 mg/kg. Groups are illustrated in Fig. 6A. Results are presented as the mean ± SD (n = 6). n.s. indicates not significant, P > 0.05, *P < 0.05, **P < 0.01, ***P < 0.001.

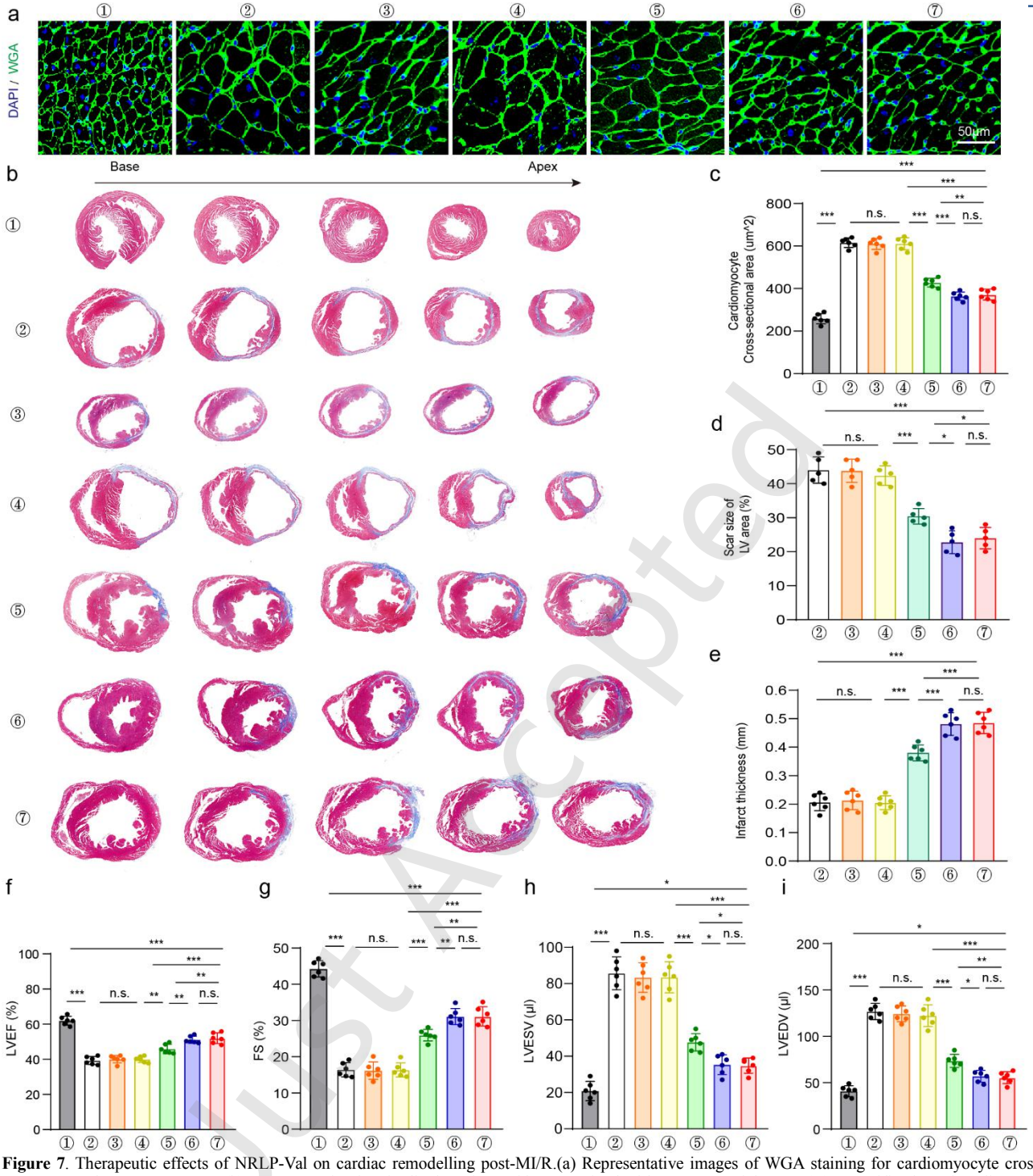

Figure 7. Therapeutic effects of NRLP-Val on cardiac remodelling post-MI/R.(a) Representative images of WGA staining for cardiomyocyte cross-sectional area at 4 weeks post-treatment. (b) Representative longitudinal sections of hearts stained with Masson's trichrome. (C) Quantification of cardiomyocyte cross-sectional area from (a). (D) Quantification of myocardial fibrosis area (percentage of total left ventricle) from Masson's trichrome staining. (e) Measurement of infarct wall thickness from Masson's trichrome. (f–i) Echocardiographic assessment of cardiac function and remodelling at 4 weeks: left ventricular ejection fraction (LVEF, f), fractional shortening (FS, g), left ventricular end-systolic volume (LVESV, h), and left ventricular end-diastolic volume (LVEDV, i). Groups are illustrated in Fig. 6A. Results are presented as mean ± SD (n = 6). n.s. indicates not significant, $P > 0.05$, *$P < 0.05$, **$P < 0.01$, ***$P < 0.001$.

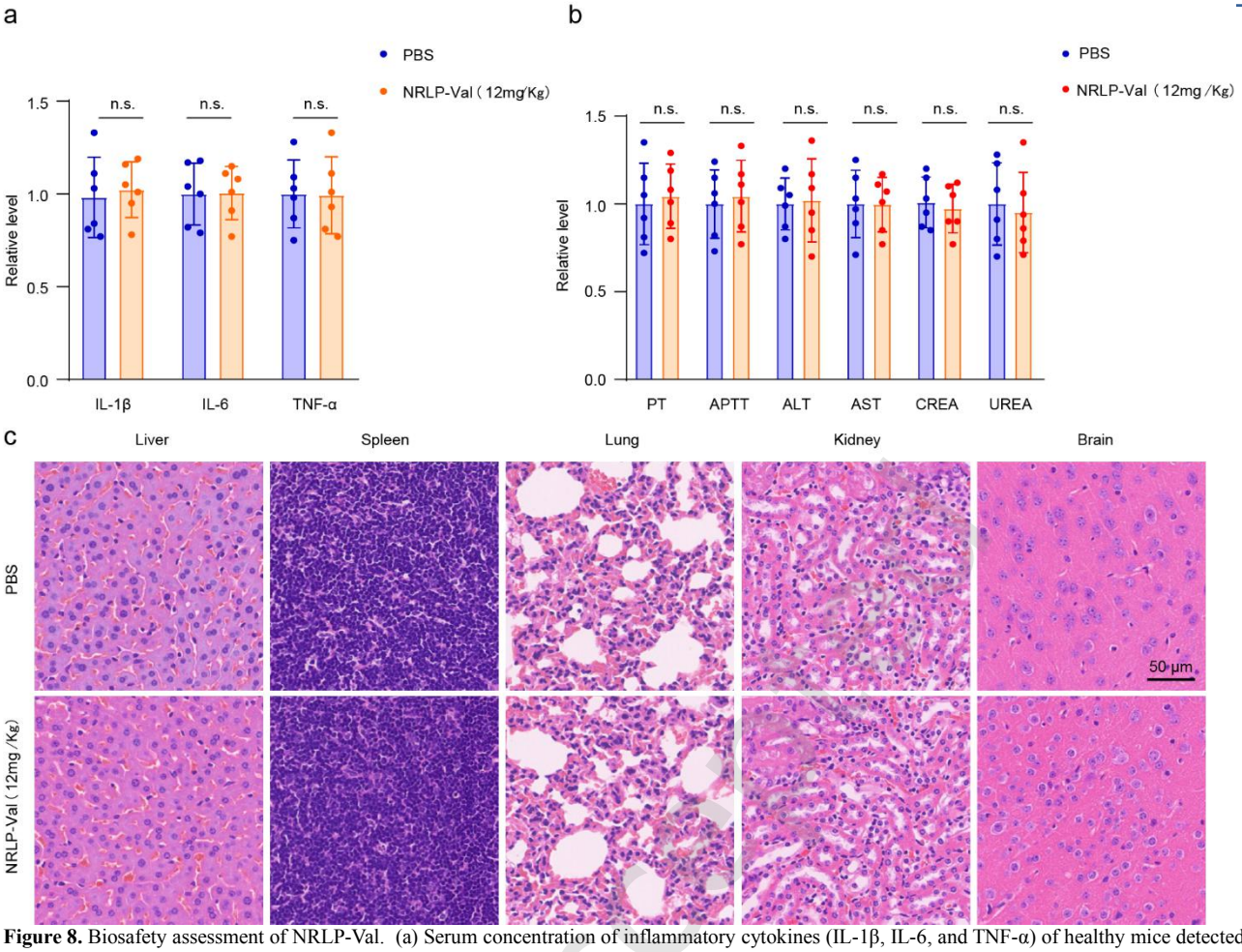

Figure 8. Biosafety assessment of NRLP-Val. (a) Serum concentration of inflammatory cytokines (IL-1β, IL-6, and TNF-α) of healthy mice detected by ELISA assay at 3 d post administration of PBS or NRLP-Val (12 mg/kg) (n = 6). (b) Evaluation of the effect of PLP-RvD1 on clotting function (PT and APTT), liver function (ALT, AST) and renal function (CREA, UREA) of healthy mice after PBS or NRLP-Val (12 mg/kg) administered (n = 6). (c)Representative images of HE staining of major organs, including liver, spleen, lung, kidney and brain. Results are presented as mean ± SD, n.s. indicates not significant, $P > 0.05$

Electronic Supplementary Material

Decoupling local renin-angiotensin system inhibition from systemic effects: A neutrophil-mimetic, ROS-responsive nanocarrier for precision therapy of myocardial ischemia/reperfusion injury

Wusiman Yakufu[1,2,§], Yuekai Shi[3,§], Jinfeng Gao[3,§], Ayitongguli Aimaiti[1,2], Nueraili Kadi[1,2], Qiyu Li[3], Miribanguli Alifu[1,2], Aikebaier Yasen[5], Muhetaer Wubuli[1,2], Yang Pang[1,3], Su Li[3], Zhenzhen Huang[1,2], Rongrong Lu[1,2], Maimaitiaili Tuerxun[1,2], Reyimai Mutailipu[1,2], Abulimiti Jamali[1,2], Wumaierjiang Kelimu[1,2], Xianglin Tang[3], Qibing Wang[3], Yuqiong Chen[4]✉, Abudureheman Mijiti[1,2]✉, Zheyong Huang[3]✉, and Junbo Ge[3]

1 Kashi Prefecture Second People's Hospital, Kashi 844000, China

2 The First Affiliated Hospital of Kashi University, Kashi 844000, China

3 Department of Cardiology, Zhongshan Hospital, Shanghai Institute of Cardiovascular Diseases, Fudan University, Shanghai 200032, China

4 The Affiliated Suzhou Hospital of Nanjing Medical University, Suzhou 215000, China;

5 Kashi University School of Medicine, Kashi 844000, China

§Wusiman Yakufu, Yuekai Shi, and Jinfeng Gao contributed equally to this work.

✉Address correspondence to Abudureheman Mijiti, 18999199903@163.com; Zheyong Huang. zheyonghuang@126.com; Yuqiong Chen, cosmoscyq@163.com

Supporting information to https://doi.org/10.26599/NR.2026.94908732

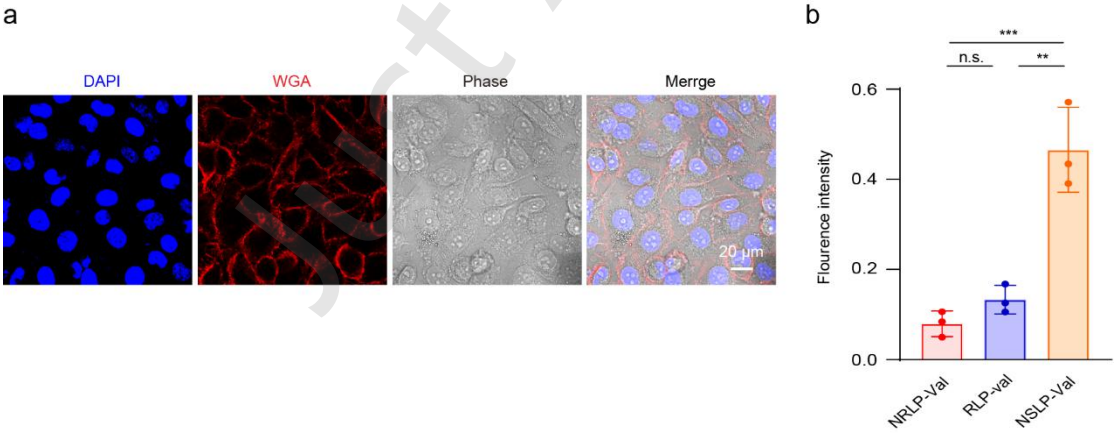

Figure S1. Assessment of endothelial monolayer integrity and nanoparticle translocation in the transwell model. (a) Representative fluorescence image of HUVECs stained with wheat germ agglutinin (WGA), confirming the formation of a confluent monolayer. (b) Quantitative analysis of fluorescence intensity in the upper and lower chambers of the transwell system following incubation with DiD-labeled RLP-Val or NRLP-Val, with or without LPS pretreatment of HUVECs(n=3). Results are presented as the mean ± SD. n.s. indicates not significant, $P > 0.05$, $^{**}P < 0.01$, $^{***}P < 0.001$.

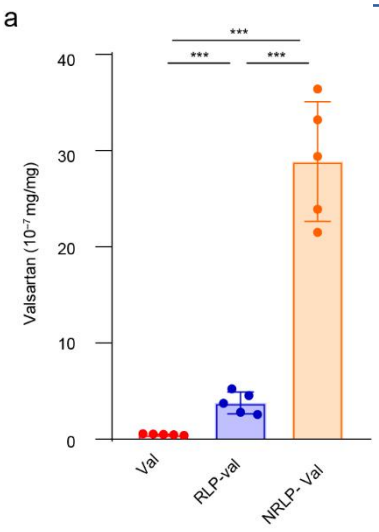

Figure S2. Quantitative assessment of valsartan delivery to cardiac tissue post-MI/R. The concentration of valsartan in heart tissues of MI/R mice was determined via high-performance liquid chromatography (HPLC) at 12 hours post-injection of free valsartan, RLP-Val, or NRLP-Val (n=6). Results are presented as the mean ± SD. ***P < 0.001.

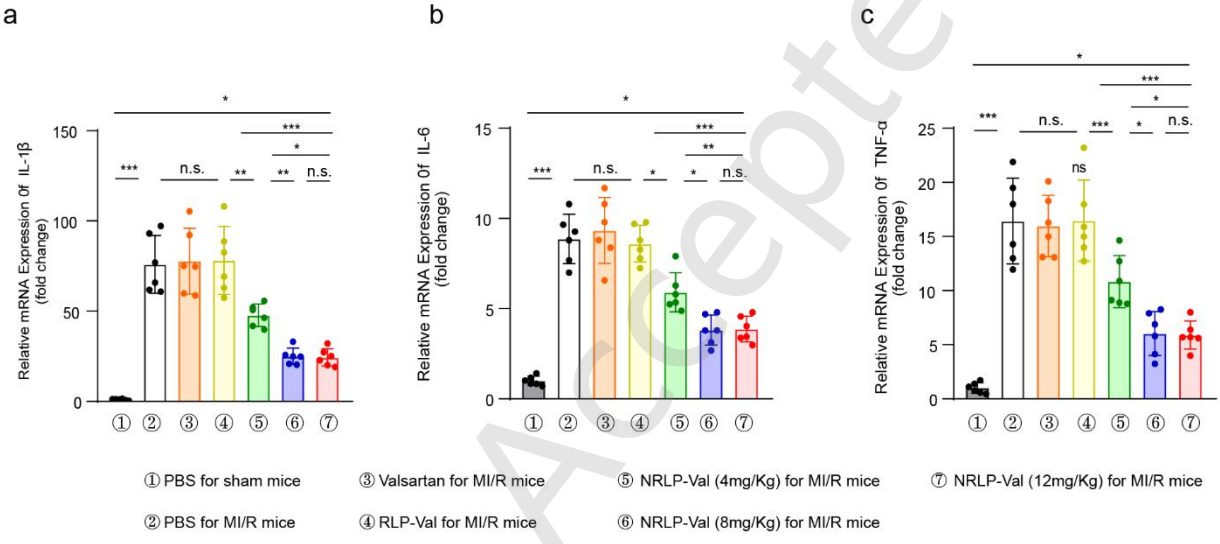

Figure S3. Expression of pro-inflammatory cytokines in cardiac tissue following MI/R. Real-time quantitative PCR analysis of mRNA expression levels of (a) IL-1β, (b) IL-6, and (c) TNF-α in heart homogenates from sham-operated mice or MI/R mice at 3 days after treatment with PBS, free Valsartan, RLP-Val, or NRLP-Val at doses of 4, 8, and 12 mg/kg (n = 6). Results are presented as the mean ± SD. n.s. indicates not significant, P > 0.05, *P < 0.05, **P < 0.01, ***P < 0.001.